SKIN FRICTION CHARACTERISTICS IN SMOOTH-WALL, TRANSITIONALLY ROUGH AND FULLY ROUGH TURBULENT BOUNDARY LAYER

BY

Mohammad Khalid Shah

A Thesis
Submitted to the Faculty of Graduate Studies
In Partial Fulfillment of the Requirements for the Degree of

Master of Science
In
Mechanical Engineering

Department of Mechanical and Manufacturing Engineering
University of Manitoba
Winnipeg, Manitoba
Canada

THE UNIVERSITY OF MANITOBA

FACULTY OF GRADUATE STUDIES

*****

COPYRIGHT PERMISSION

SKIN FRICTION CHARACTERISTICS IN SMOOTH-WALL, TRANSITIONALLY ROUGH AND FULLY ROUGH TURBULENT BOUNDARY LAYER

BY

Mohammad Khalid Shah

A Thesis/Practicum submitted to the Faculty of Graduate Studies of The University of Manitoba in partial fulfillment of the requirement of the degree

Of

MASTER OF SCIENCE

ABSTRACT

This thesis presents an experimental investigation of skin friction characteristics in zero-pressure gradient turbulent boundary layers over a smooth surface, and transitionally rough and fully rough surfaces. The rough surfaces were created from three geometrically different roughness elements namely perforated plate, sand paper and wire mesh. The velocity measurements were obtained using a Pitot-probe. The Reynolds number based on the freestream velocity (U_e) and momentum thickness (θ) were in the range $2700 \leq \mathrm{Re}_\theta (=U_e\theta/\nu) \leq 7900$. The classical log law and the power law proposed by George and Castillo (1997) were applied to process the mean velocity profile and to obtain the corresponding skin friction values. For the smooth surface, the fringe imaging skin friction technique was also applied to obtain independent skin friction values, and the results were compared with values determined from the log law and power law. The results demonstrate that the skin-friction values obtained from the log law and power law are in reasonable agreement with those determined from the fringe imaging skin friction technique. However, the power law describes a substantially larger extent of the mean velocity profile than the log law, as expected. The mean velocity defect profiles show distinct Reynolds number and roughness effects when scaled with the freestream velocity (U_e) and the friction velocity (U_τ). However, the defect profiles obtained at various Reynolds number and geometrically different surfaces collapse reasonably well when scaled with the mixed scaling ($U_e\delta^*/\delta$). The results also show that the strength of wake obtained for rough surfaces were higher when compared to values obtained for smooth surfaces.

ACKNOWLEDGEMENTS

My first and foremost thanks go to Allah Almighty for bringing me this far in life. I would like to express my sincere appreciation and gratitude to my advisor Dr. Mark F. Tachie for giving me the opportunity to work in this challenging field of research. His invaluable help with all aspects of this thesis as well as with my graduate course work is greatly appreciated.

I would like to thank my parents, Idrees and Kauser Shah, brothers, Tariq and Omer Shah, and my sister-in-law, Sabuhi Shah, who gave me a lot of support, financially and spiritually that helped me to be here and finish my thesis. I would also like to thank my fiancée, Aysha and her parents, Wajid and Najma Hussain, for their encouragement and understanding. I am also grateful to Mr. Maher Abou Al-Sood, Kofi Adane, Martin Agelinchaab, Samuel Paul, Qing Sun, Preshit Upadhye, Anil Voodi, and Ms. Shannon Summerfield for their support during the course of my study. Technical assistance provided by John Finken is gratefully acknowledged.

I would like to thank Dr. Donald J. Bergstrom, Dr. David Sumner, Olajide Akinlade and Dave Deutscher at University of Saskatchewan for assisting me in gathering data for the mean velocity measurements. I also wish to acknowledge Dr. Gregory G. Zilliac (Ames Research Centre) for providing the FISF software and manual.

Funding for the project was provided through National Sciences and Engineering Research Council of Canada Discovery Grant and University of Manitoba Research Grant Program to Dr. Mark F. Tachie.

DEDICATION

This thesis is dedicated to my parents, M. Idrees and Kauser Shah, for giving me the necessary support to pursue my studies.

TABLE OF CONTENTS

LIST OF TABLES

LIST OF FIGURES

NOMENCLATURE

ENGLISH SYMBOLS

C : Additive constant in log law

C_f : Skin friction coefficient

C_i : Power law multiplicative factor

C_o : Power law multiplicative factor

D : Additive constant in log law

H : Shape factor

k : Roughness height (mm)

k^+ : Roughness Reynolds number

k_s : Equivalent sand grain roughness (mm)

k_s^+ : Reynolds number based on equivalent sand grain roughness

q : Dynamic pressure

Re : Reynolds number

Re_θ : Reynolds number based on momentum thickness

Re_k : Reynolds number based on roughness height

Δs : Distance between two destructive interference bands

U : Streamwise component of mean velocity (m/s)

U_e : Freestream velocity (m/s)

U_τ : Friction velocity (m/s)

U^+ : Normalized velocity

ΔU^+ : Roughness function

ΔU^{+}_{max} : Maximum deviation of a profile above the log law

x : Streamwise distance (mm)

y : Vertical or wall-normal distance (m)

GREEK SYMBOLS

γ : Power law exponent

δ : Boundary layer thickness (mm)

δ^{*} : Boundary layer displacement thickness (mm)

δ^{+} : Reynolds number based on boundary layer thickness and friction velocity

ε : Virtual origin (mm)

θ : Boundary layer momentum thickness (mm)

κ : Von Karman constant

λ : Wavelength

μ : Absolute viscosity ($N.s/m^2$)

ν : Kinematic viscosity (m^2/s)

Π : Strength of wake

ρ : Density (kg/m^3)

τ_w : Wall shear stress (N/m^2)

SUPERSCRIPTS

+ : Normalized by viscous unit

SUBSCRIPTS

o : Oil

CHAPTER 1: INTRODUCTION

1.1 General Remarks

The study presented in this thesis pertains to the experimental investigation of turbulent boundary layers. Specifically, the characteristics of hydrodynamically smooth, transitionally rough and fully rough wall turbulent boundary layers are examined. An insightful interpretation of the results presented in this thesis requires the boundary layer concept and important parameters be examined first. As is well known, rough wall turbulent boundary layers are significantly more complex than smooth wall boundary layers. Therefore, the characteristics of rough wall turbulent boundary layer flows are also discussed. The importance of accurate determination of the skin friction is discussed and the various skin friction measurement techniques are summarized.

1.2 Boundary Layer Concept

Ludwig Prandtl, a German aerodynamicist, first introduced the concept of boundary layer in 1904. The concept of the boundary layer is considered a breakthrough in the field of fluid mechanics and facilitated the theoretical treatment of viscous flows. Although the complete equations describing the motion of a viscous fluid (the Navier-Stokes equations, developed by Navier, 1827, and independently by Stokes, 1845) were known prior to Prandtl, the mathematical difficulties in solving these equations (except for a few simple cases) prohibited a theoretical treatment of viscous flows. The boundary layer concept provided the link that had been missing between theory and practice.

If a flow moves parallel to a surface such as a flat plate, the plate retards the oncoming flow. The viscous effects at the wall brings the fluid to a halt, and then slowly moving particles retard their neighbors above, so that a distance away from the leading edge of the plate, there is a significant retarded shear layer, or a *boundary layer* of thickness δ.

Prandtl showed that the boundary layer can be analyzed by dividing the flow into two regions, one close to the solid boundary, and the other covering the rest of the flow. Only in the thin region adjacent to the solid boundary is the effect of viscosity important. In the region outside of the boundary layer, the effect of viscosity is negligible and the fluid may be treated as inviscid. Thus the introduction of the boundary-layer concept marked the beginning of an important era of fluid mechanics.

Boundary layer theory has many important applications, for example, the calculation of skin-friction drag which acts on a body as it moves through a fluid. Typical examples are the calculations of the skin-friction drag on lifting surface and airplane bodies, ship hulls, and on the turbine blade and rotary compressors. Boundary layer theory is also related to the process of convective heat and mass transfer which have applications in industrial operations, fuel droplet evaporation and condensation on a cool surface.

1.2.1 Integral Thicknesses and Shape Factor

The displacement thickness (δ^*) and the momentum thickness (θ) are recognized as integral thicknesses.

A small but finite displacement of the outer streamlines takes place in the boundary layer. As shown in Figure 1-1, outer streamlines must deflect outward a distance δ^* to satisfy conservation of mass between the inlet and outlet. This quantity is called the *displacement thickness* (δ^*) of the boundary layer. For an incompressible flow the displacement thickness is given by,

$$\delta^* = \int_0^{\delta} (1 - \frac{U}{U_e}) dy \tag{1.1}$$

Since, $U = U_e$ at $y = \delta$, the integral is essentially zero for $y \geq \delta$.

The *momentum thickness*, θ, is defined as the thickness of the layer of fluid, of velocity U_e, for which the momentum flux is equal to the deficit of momentum flux through the boundary layer. For an incompressible flow, the momentum thickness is given by,

$$\theta = \int_0^{\delta} \frac{U}{U_e} (1 - \frac{U}{U_e}) dy \tag{1.2}$$

Again, the integral is essentially zero for $y \geq \delta$.

The displacement and momentum thickness are appreciably easier to evaluate accurately from experimental data than the boundary layer thickness δ. This fact,

combined with their physical significance accounts for their common use in specifying boundary-layer parameters.

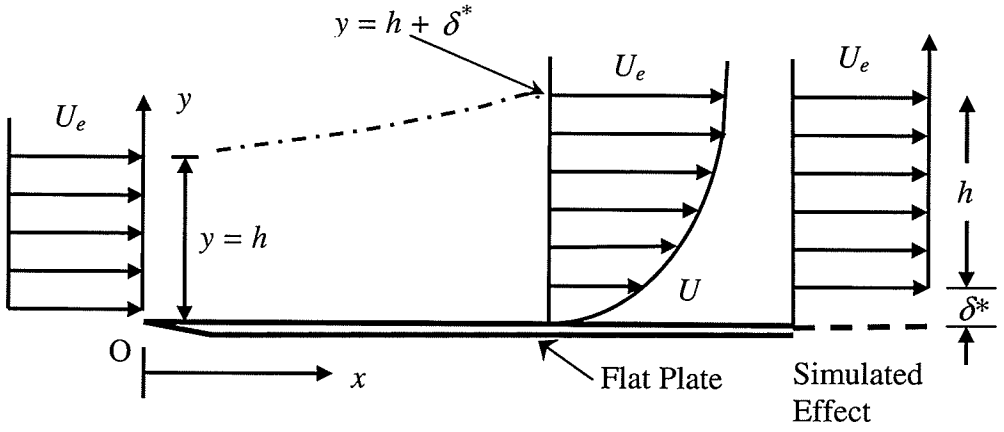

Figure 1-1: Displacement effect of a boundary layer (White, 1986).

The momentum thickness is often used to correlate data taken from a variety of boundary layers under different conditions. The ratio of displacement thickness to momentum thickness gives the dimensionless-profile shape factor:

$$H = \frac{\delta^*}{\theta} \tag{1.3}$$

1.2.2 Reynolds Number

The importance of the Reynolds number was recognized earlier by Stokes but it has come to be termed Reynolds number in recognition of Osborne Reynolds demonstrating its effect on the onset of turbulence (Reynolds, 1883).

Reynolds number is the ratio of inertia forces (non-linear) to the viscous (linear) forces. The inertia forces are responsible for the flow instability, while the viscous forces convert the kinetic energy into thermal energy. If L and U are the characteristic length

and velocity scales, respectively, and ν is the kinematic viscosity, then the Reynolds number is given by

$$\mathrm{Re} = \frac{UL}{\nu}. \tag{1.4}$$

This seemingly superficial non-dimensionalization reveals two important properties. The first is the concept of *dynamic similarity*. That is, no matter how L, U and ν are varied, as long as the Reynolds number is the same in two geometrically similar flows, they have the same solution. Small-scale model testing of large-scale real-life flows is based on this property. Secondly, for a given geometry and boundary condition, the effect of changing L, U, or ν or any combination of them, can be described uniquely by the change of Reynolds number alone.

In near-wall turbulence applications, variations of Reynolds numbers are used such as, Reynolds number based on momentum thickness Re_θ (= $U_\infty\theta/\nu$); Reynolds number based on average roughness height (k) and friction velocity (U_τ) Re_k (= $U_\tau k/\nu$) and Reynolds number based on boundary layer thickness and friction velocity δ^+ (= $U_\tau\delta/\nu$).

1.3 Reynolds Number Effects

The range of Reynolds numbers achievable in physical and numerical experiments, as well as those encountered in engineering applications are illustrated in Figure 1-2. It can be observed that the Reynolds numbers encountered in many practical situations are typically orders of magnitude higher than those studied computationally and/or

experimentally. However, our knowledge of high-Reynolds number flows is very limited and a complete understanding is yet to emerge. Direct Numerical Simulation (DNS) modeling capabilities are limited and not yet powerful enough to solve high Reynolds number problems. At present, very few existing experimental facilities can deliver the ultra-high Reynolds number flows while maintaining relatively low Mach number (to avoid compressibility effects). The world's largest wind tunnel, Aerodynamic Facility at NASA Ames, is capable of generating a boundary layer with a momentum thickness Reynolds number (Re_θ) $3.7x10^5$ (Saddoughi and Veeravalli, 1994). These large scale facilities are relatively expensive to build and operate and the ones existing are heavily scheduled with developmental work.

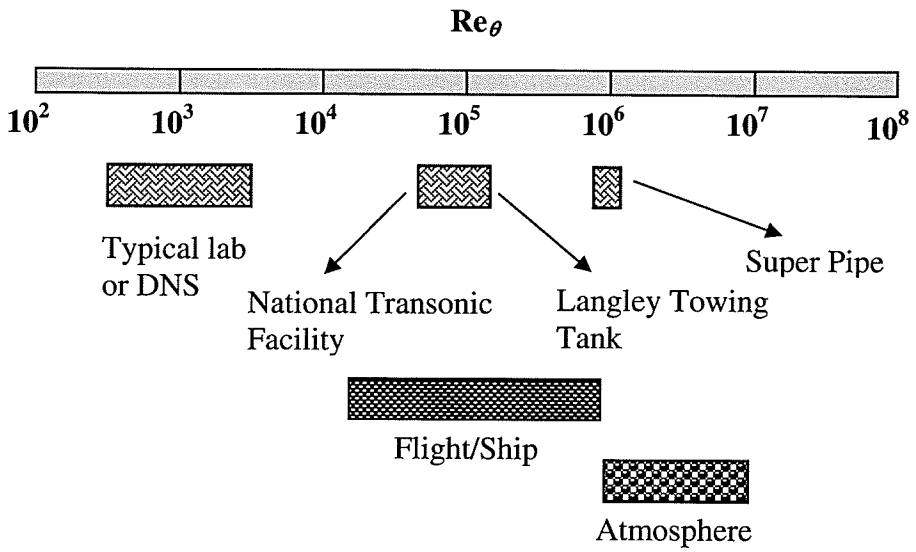

Figure 1-2: Ranges of momentum-thickness Reynolds number for different facilities and for field conditions (Gad-el-Hak and Bandyopadhyay, 1994).

A vast amount of energy is spent in overcoming the turbulence skin-friction drag in pipelines and on air, water and land vehicles. For example, skin friction can be a large

portion of a vehicle's drag and is responsible for up to 50% of the drag at cruise for conventional aircraft. The skin friction characteristics as well as mass and convective heat transport depend on the Reynolds number. Hence, it is of great practical importance to understand the effects of Reynolds number on the turbulent boundary layers. A better understanding of Reynolds number effects on skin friction and other boundary layers parameters will allow the extrapolation of important parameters such as skin friction obtained from low Reynolds number to high Reynolds number of practical importance. Reynolds number effects on turbulent boundary layers will be discussed in detail in chapter 2.

1.4 Turbulent Flow over Rough Surfaces

Turbulent flows over rough surfaces are prevalent in the fields of marine, aeronautical, and hydraulic engineering applications. For example, environmental flows involving the dispersion of waste in rivers and stream beds are always rough. It should be noted that even if the surface of interest was indeed manufactured to be aerodynamically smooth, degeneration due to a number of factors (nature, usage, etc.) will often degrade the smoothness of the surface. Turbine blades are an example of such surfaces which were initially manufactured smooth but could roughen over time. Other examples of rough surfaces encountered in practical engineering include rivet heads, welded seams and joints found on ships and airplanes.

Turbulent boundary layers over rough surfaces have considerable engineering interest due to the increased transport of heat, mass and momentum (Krogstad and

Antonia, 1999). For example, the pronounced effect of certain paints upon the measured drag of full-scale vessels may increase the surface resistance by 50% or cause an increase in total drag by 25% compared to clean/smooth ships (Todd, 1951).

1.4.1 Definitions and Terminology

For a rough surface, the wall boundary condition becomes more complex than a flat plate boundary layer because the flow is no longer parallel to the ground plane. Instead, details of the flow in the roughness sublayer depend on the specific geometry of the roughness elements (Bergstrom *et al.*, 2002). For example, in the case of roughness configurations which resemble bluff body structures attached to a ground plane, the flow structure is dominated by the wakes created by the roughness elements.

It is deemed useful to give a brief introduction of the notations and terms used in this and subsequent chapters for discussing roughness effects. Figure 1-3a shows a schematic illustration of a rough wall along with some geometrical features of the roughness elements. For a rough wall turbulent boundary layer, the average roughness height is denoted by k; y_p is the wall normal distance measured from the top plane of the roughness element; ε is the virtual origin and represents the distance between y_p and the location at which the mean velocity goes to zero (i.e., $U = 0$). Therefore, for a rough surface, the effective wall normal distance $y = y_p + \varepsilon$. For a given roughness height, the virtual origin must satisfy the following constraint: $0 < \varepsilon < k$. The exact value of ε, however, depends on the roughness elements and other geometric factors such as size, distribution, density and shape.

Since there can be infinite number of possible surface states, it is customary in technical applications to introduce a standard roughness that can be used to describe the effect of roughness on the flow. It is assumed that a rough wall can be treated as a surface that is covered with a layer of closely packed spheres like a sand paper. Therefore, it is called *sand-roughness*. The diameter of the spheres is called the sand roughness height k_s and is a measure of the surface roughness of the wall. An illustration of sand roughness height is shown in Figure 1-3b. Any technical roughness element can be generally assigned to a so-called *equivalent sand roughness* $k_s^+ (= k_s U_\tau / \nu)$.

For a rough wall turbulent boundary layer, the term *roughness sublayer* indicates the entire layer dynamically influenced by length scales associated with roughness elements. Roughness sublayer exists below the inertial or logarithmic layer and is the rough-wall counterpart to the viscous sublayer over a smooth wall.

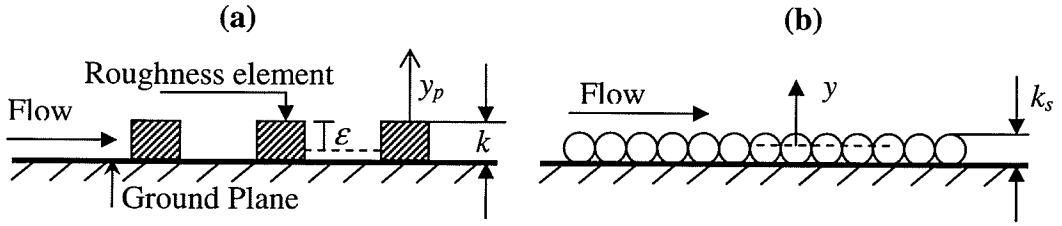

Figure 1-3: a) Definition sketch of roughness elements; b) Sand roughness height k_s.

1.4.2 Roughness Regimes

If the roughness elements are so small that the viscous sublayer enclosing them is stable against any perturbation, the roughness will have no drag-increasing effect. This is called the *hydrodynamically smooth* case. In hydrodynamically smooth flow the viscous

sublayer is dominated by viscous effects. The flow characteristics over hydrodynamically smooth surfaces are principally controlled by Reynolds numbers.

If the roughness elements extend in the overlap layer, i.e. fill up practically the entire viscous sublayer and most of the inner layer, viscosity effects vanish. Hence, the surface resistance will then be independent of the viscosity. This is called the *fully rough regime*. For a fully rough regime the flow is independent of viscosity or Reynolds number and depends only on k_s^+ (Schlichting, 1968).

Between these two extremes there exists an intermediate regime in which the roughness elements cover the viscous sublayer but only cover a fraction of the overall inner layer. This is a case of *transitionally rough regime*. The characteristics of transitionally rough flow regimes depend on both the Reynolds number and k_s^+. Therefore, it is not surprising that the characteristics of this type of regime are the most difficult to generalize and also the one that are least understood among the three regimes.

According to White (1991), $k_s^+ < 4$ corresponds to hydrodynamically smooth surface, $k_s^+ > 60$ corresponds to fully rough regime, and $4 \leq k_s^+ \leq 60$ corresponds to transitionally rough regime. In this thesis, the classification of White (1991) is used for characterizing the roughness regimes.

1.5 Applications of Skin Friction Data

The skin friction characteristics of turbulent boundary layer have been studied extensively and remains a very important research topic. The ever-increasing importance of skin friction measurements is due to its wide range of applications. As skin friction measurement becomes easier and the accuracy of the results increases, it is expected that the number of applications taking advantage of skin friction will grow.

Accurate skin friction is also important from the point of view of fundamental near-wall turbulence research. For example, the skin friction is important because most of the scaling laws proposed for the boundary layer analysis involve the friction velocity (equivalent of skin friction) or wall shear stress. Skin-friction is also essential for the validation of near-wall turbulence models. In other words, skin friction is more difficult to predict by turbulent models than are other quantities, such as pressure. Therefore, skin friction data will eventually be the validation quantity of choice, as detailed and accurate skin friction measurements become more readily available. An example of the use of skin friction measurements for validation of numerical models is the comparative study of the ability of different CFD codes and turbulence models to calculate the flow fields around shock wave/boundary layer interactions (Knight and Degrez, 1998). In some of these cases, quantities such as wall pressure and surface streamline are predicted accurately, but the wall shear stress is grossly over or under predicted.

The skin friction parameter is also of primary importance from a practical perspective since it is related to the viscous drag force. Therefore, in most applications of

fluid mechanics knowledge of the skin friction created by fluid flowing over a surface is essential to the understanding of the performance of fluid engineering system such as a ship or an aircraft or the flow through a pipe. The importance of skin friction data in aerodynamic testing has also stimulated a continuing effort to develop reliable instrumentation for its measurement. For example, aerodynamicists would like to know where the skin friction levels are high, where transition occurs and if separation is present.

Given the wide range of applications, various techniques have been developed for the measurement of skin friction. These techniques can be broken down into two categories: 1) direct skin friction measuring techniques and 2) indirect skin friction measuring techniques.

Direct skin friction measuring techniques include, oil film interferometery techniques (i.e., fringe imaging skin friction technique), liquid crystal coating techniques, and floating point element techniques. The Preston tubes, profile matching techniques (i.e., Clauser plot, power law) and momentum balance method are examples of indirect skin friction measurement techniques. Haritonidis (1989), Winter (1997) and Naughton and Sheplak (2002) provide comprehensive reviews of the various skin-friction measurement techniques. Even though a lot of techniques are available for measuring skin friction, it should be realized that some of these methods are either time consuming or intrusive or require exhaustive calibration.

Profile matching techniques are widely used in wind tunnel experiments to obtain reasonable values of skin friction. Profile matching techniques such as Clauser plot (based on log law) and power law are applicable over a wide range of boundary. At present there is no consensus on whether the log law or the power law is more appropriate for describing mean velocity profile in the overlap region. The classical log law has been proven to be very effective as a universal curve for the inner region of the canonical boundary layer. Only recently, have doubts begun to arise about its validity. The main question is whether the log law which is Reynolds number independent or a power law with Reynolds number dependence is more appropriate.

1.6 Objectives

The purpose of this research is to apply various methods to study skin friction characteristics of zero pressure gradient turbulent boundary layers in hydrodynamically smooth, transitionally rough and fully rough regimes. The specific objectives are as follows

1. To apply the classical log law and the power law proposed by George and Castillo (1997) to determine the skin friction in a smooth-wall turbulent boundary layer.

2. To apply an independent technique known as Fringe Imaging Skin Friction Technique for smooth surfaces that does not depend on the validity of the log law or power law to determine the skin friction. To compare these results with those determined from the log law and power law and determine the appropriateness of the two laws.

3. To apply the log law and power law to study the skin friction characteristics of both transitionally rough and fully rough surfaces generated from geometrically different roughness elements.

CHAPTER 2: LITERATURE REVIEW

Relevant literature pertaining to a turbulent boundary layer is reviewed. Specifically, the scaling laws for the inner and outer regions of the mean velocity profile are discussed. The log law and power law proposed by George and Castillo (1997) are reviewed and theoretical basis of Fringe Imaging Skin Friction technique (FISF) is summarized. Prior mean velocity measurements on smooth and rough surfaces and also the procedure used to determine the friction velocity are reviewed.

2.1 Theoretical Analysis

2.1.1 Structure of Turbulent Boundary Layer

The techniques utilized for measuring skin friction rely directly or indirectly on the structure of the turbulent boundary layer. Hence, it is deemed useful to give a brief review of the structure of a turbulent boundary layer based on the current understanding.

A typical boundary layer profile can be divided into two distinct layers; namely *the inner layer* and *the outer layer.* At sufficiently high Reynolds numbers, classical theories, for example, asymptotic expansion (Milikan, 1938) and mixing length (Prandtl, 1932), suggest an *overlap region* between the inner and outer layers. The extent of the various regions in terms of wall variables is illustrated in Figure 2-1. Here and elsewhere, superscript '+' is used to represent quantities in wall variables. For example, $U^+ = U/U_\tau$, and $y^+ = yU_\tau/\nu$, where, $U_\tau (=\sqrt{(\tau_w/\rho)}$, τ_w is the wall shear stress and ρ is the density) is the friction velocity and ν is the kinematic viscosity.

Viscosity plays an important factor in the *inner layer*. As shown in Figure 2-1, the inner region consists of the viscous sublayer, the buffer region and the overlap region. The velocity profiles varies linearly with distance from the wall (i.e., $U^+ = y^+$) in the viscous sublayer. The viscous sublayer is also known as the linear region and extends from $0 \leq y^+ \leq 5$ while the buffer region extends from $5 \leq y^+ \leq 30$. The *outer layer* of the boundary layer is dominated by inertia forces and extends from $30 \leq y^+ \leq \delta^+$. The *overlap region* ($30 \leq y^+ \leq 0.2\delta^+$) is obtained where both the inner layer and outer layer simultaneously exist. Hence, it possesses the characteristics of both the inner and the outer layer.

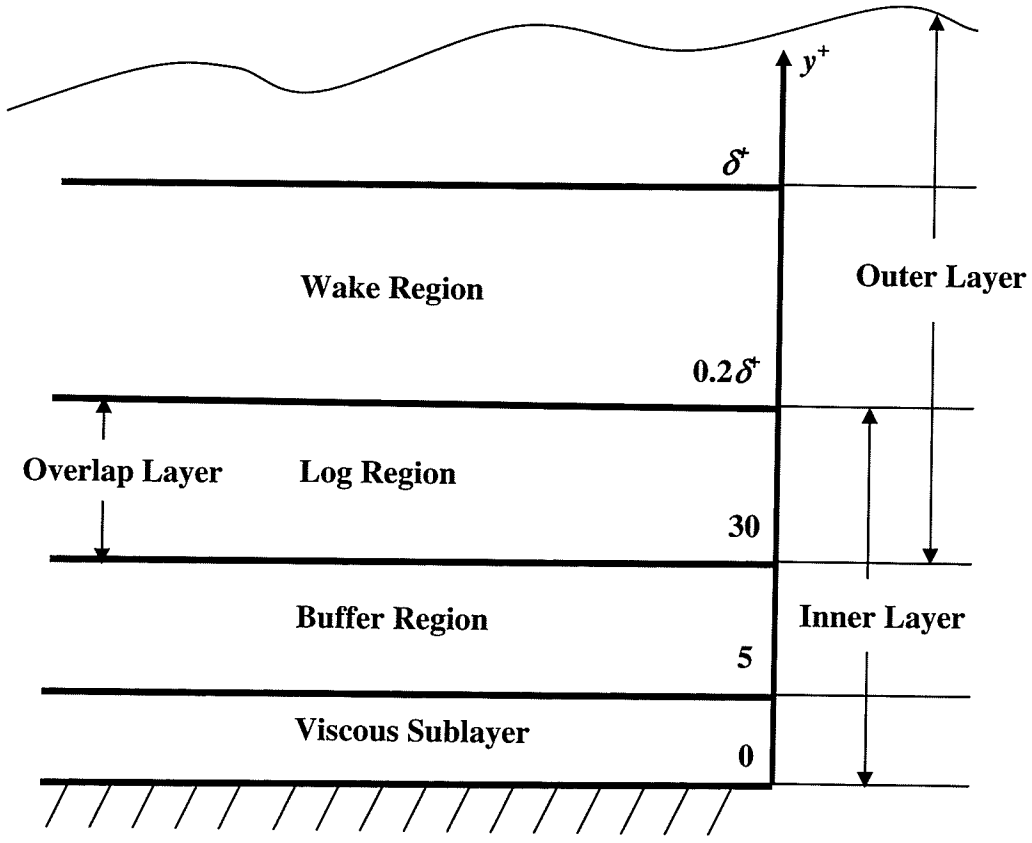

Figure 2-1: Schematic of different regions in a typical turbulent boundary layer profile (Gad-el-Hak and Bandyopadhyay, 1994).

2.1.2 The Turbulent Boundary Layer Equations

Prandtl first proposed the boundary layer equations by simplifying the two dimensional incompressible Navier-Stokes equations for steady flows. For a boundary layer, it is assumed that $\delta << L$ (δ is the boundary layer thickness and L is the characteristic length of the plate). It follows from the order of magnitude analysis that $\partial/\partial x << \partial/\partial y$, thus for zero pressure gradient (ZPG), incompressible turbulent boundary layer, the governing equations become,

$$\frac{\partial U}{\partial x}+\frac{\partial V}{\partial y}=0 \tag{2.1}$$

$$U\frac{\partial U}{\partial x}+V\frac{\partial U}{\partial y}=\frac{\partial}{\partial y}\left[-<uv>+\nu\frac{\partial U}{\partial y}\right]+\frac{\partial}{\partial x}[<v^2>-<u^2>] \tag{2.2}$$

where, $U \rightarrow U_e$ at $y \rightarrow \infty$ and $U = 0$ at $y = 0$. The presence of the no-slip condition rules out the possibility of similarity solutions for the entire boundary. However, in the range of infinite Reynolds number, the viscous terms vanish and the solutions to the equations of motion fail to satisfy the boundary conditions. Therefore, the boundary layer is divided into two regions: the outer layer where viscous effects are negligible and the inner layer where viscous effects dominate, but the inertia terms vanish in this limit as mentioned earlier.

The boundary layer equations can be described asymptotically in the outer region as follows:

$$U\frac{\partial U}{\partial x}+V\frac{\partial U}{\partial y}=\frac{\partial}{\partial y}[-<uv>]+\frac{\partial}{\partial x}[<v^2>-<u^2>] \tag{2.3}$$

The governing equation for the inner region is as follows

$$0 = \frac{\partial}{\partial y}\left[- < uv > + \nu \frac{\partial U}{\partial y} \right], \tag{2.4}$$

which covers the region between $y^+ = 0$ and $y^+ = 0.2\delta^+$. In Eqn. 2.3 for the outer region, $<v^2>$ and $<u^2>$ are neglected from the similarity analysis for ZPG flow. Also at the wall, where the turbulent shear stress is zero, the wall shear stress is given by

$$\tau_w = \mu \left. \frac{\partial U}{\partial y} \right|_{y=0} . \tag{2.5}$$

2.1.3 Scaling Law for the Inner Layer

In the classical approach, dimensional analysis of the dynamic equation and boundary conditions lead to a scaling law for the mean velocity profile. The distance from the wall (y), the wall shear stress (τ_w) and the fluid properties, i.e., kinematic viscosity (ν) and density (ρ) dictate the flow dynamics in the immediate vicinity of a solid boundary.

From dimensional considerations, the following dimensionless functional relationship is obtained for the mean velocity

$$\frac{U}{U_\tau} = f_i\left[\frac{yU_\tau}{\nu}, \frac{\delta U_\tau}{\nu} \right] \tag{2.6}$$

or

$$U^+ = f_i[y^+, \delta^+], \tag{2.7}$$

where U_τ is the friction velocity and δ^+ is a Reynolds number based on the boundary layer thickness (δ) and the friction velocity and indicates the ratio of the outer to inner

length scales. If the dimensionless functional relationship f_i is independent of Reynolds number, i.e.,

$$U^+ = f_i[y^+] \tag{2.8}$$

it implies complete similarity exists in the inner region. Eqn. 2.8 is commonly referred to as *the universal law of the wall.*

For a rough surface, the characteristic length scales may also include the average roughness height, k, and any additional length scales needed to completely characterize the roughness. If the viscous length scale (ν/U_τ) and the average height (k) are chosen as the only relevant length scales in order to preserve the generality of flow over both smooth and rough surfaces (Raupach *et al.*, 1991), one can define a roughness Reynolds number, Re_k (= kU_τ/ν).

2.1.4 Scaling of the Outer Layer

In the outer region, the local velocity is independent of viscosity (ν) but still dependent on the distance from the wall (y), the boundary layer thickness (δ) and a velocity scale (U_o). Unlike the inner layer, no equivalent theory has been proposed by the classical theories for the outer layer. Instead, it is assumed that the friction velocity is the appropriate velocity scale (i.e., $U_o = U_\tau$) and the velocity distribution is given by

$$\frac{U_e - U}{U_\tau} = f_o\left[\frac{y}{\delta}, \delta^+\right]. \tag{2.9}$$

However, the theory for a zero pressure gradient turbulent boundary layer proposed by George and Castillo (1997) showed that the appropriate scale for the outer

region is the freestream velocity (i.e., $U_o = U_e$). In this case, the velocity distribution is given by

$$\frac{U_e - U}{U_e} = f_o\left[\frac{y}{\delta}, \delta^+\right], \tag{2.10}$$

where f_o expresses the dimensionless functional relationship. If f_o is independent of Reynolds number, complete similarity exists in the outer region, i.e.,

$$\frac{U_e - U}{U_o} = f_o\left[\frac{y}{\delta}\right]. \tag{2.11}$$

A new type of mixed scaling, originally developed for the mean velocity profile in turbulent pipe flow, is also proposed by Zagarola and Smits (1998), i.e.,

$$\frac{U_e - U}{U_e(\delta^* / \delta)} = f_o\left[\frac{y}{\delta}\right]. \tag{2.12}$$

2.1.5 Overlap Region Scaling

The overlap region scaling is of considerable importance because the scaling for this region leads to accurate determination of friction velocity. However, the specific form of overlap scaling depends on the inner and outer scaling used in the matching process. It should be noted that in the overlap region, the inner length scale (ν/U_τ or k) is presumably too small to control the dynamics of the flow and the outer length scale (δ) is presumably too large to be effective (Tennekes and Lumley, 1972). In such a scenario, the dynamics of the flow are independent of all length scales except the distance from the wall (y).

2.1.5.1 The Log Law

According to classical theories (Milikan, 1938), there exists an overlap region where both the inner and the outer layers can be matched in the limit of infinite Reynolds number to obtain the following logarithmic law in the inner and outer variables, respectively

$$U^+ = \frac{1}{\kappa}\ln\left(y^+\right) + C \tag{2.13}$$

and

$$\frac{U_e - U}{U_\tau} = -\frac{1}{\kappa}\ln\left(\frac{y}{\delta}\right) + D, \tag{2.14}$$

where $y^+ = yU_\tau/\nu$ is the non-dimensional length for the inner layer, y/δ is the non-dimensional length for the outer layer, U_e is the freestream velocity and U_τ is the friction velocity. The log law constants are given by κ, C and D which are "supposedly" universal constants. However, as can be seen from Table 2-1 the values of κ and C vary considerably from researcher to researcher.

Table 2-1: Variation of constants in the log law by different researchers.

Coefficient	Clauser (1954)	Coles (1962)	Nikuradse (1932)	Zagarola (1998)	Österlund (1999)
κ	0.41	0.4	0.4	0.436	0.38
C	4.9	5.1	5.5	6.13	4.1

The values of κ and C are 0.41 and 5.0 respectively that are used in this research.

For a rough wall boundary layer, the mean velocity profile may be written in the following form

$$U^+ = \frac{1}{\kappa}\ln y^+ + C - \Delta U^+, \tag{2.15}$$

where ΔU^+ is the roughness function which represents the (parallel) shift between the smooth-wall and rough-wall velocity profiles on a semi-logarithmic plot as shown in Figure 2-2. The specific value of ΔU^+ depends on the roughness Reynolds number as well as the roughness geometry. The roughness function (ΔU^+) is essentially zero for smooth surfaces.

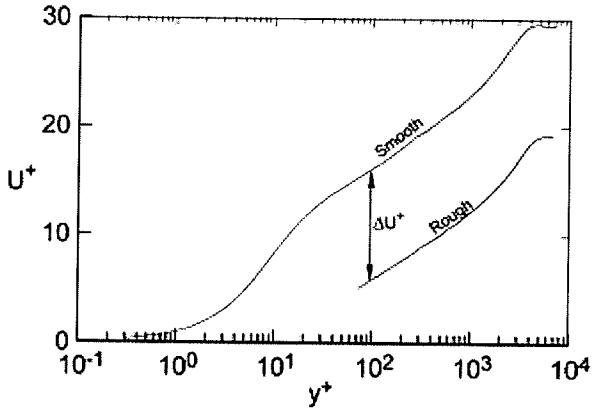

Figure 2-2: An illustration of the roughness function ΔU^+ (Krogstad and Antonia, 2001).

It is well known that the log law describes the data in a limited range ($30 \leq y^+ \leq 0.2\delta$). To describe both the overlap region and the outer layer, Coles (1956) proposed a composite mean velocity profile. This composite mean velocity profile which is given by a linear superposition of the law of the wall and the law of the wake as

$$U^+ = \frac{1}{\kappa}\ln\left(y^+\right) + C - \Delta U^+ + \frac{2\Pi}{\kappa}W\left(\frac{y}{\delta}\right), \tag{2.16}$$

where $W(y/\delta)$ is the wake function and Π represents the strength of the wake.

2.1.5.2 The Power Law

Recently, a number of power laws have been proposed as alternative to the logarithmic law (e.g. Barenblatt, 1993; George and Castillo, 1997). In this work, however, we are interested in the power law proposed by George and Castillo (1997) for a zero pressure gradient turbulent boundary layer. In their power law formulation, George and Castillo (1997) assumed complete similarity in the inner and outer layers in the limit of infinite Reynolds numbers.

It should be noted from Eqn. 2.11 that, in contrast to the classical logarithmic law (Eqn. 2.15), George and Castillo (1997) chose the freestream velocity, U_e, as the proper velocity scale for the outer layer. They applied the asymptotic invariance principle (AIP) to match inner scaling (Eqn. 2.8) and outer scaling (Eqn. 2.10) in the overlap region to obtain a power law description for the mean velocity. In inner and outer coordinates, their power law formulations are given by

$$U^+ = C_i (y^+ + a^+)^\gamma \tag{2.17}$$

and

$$\frac{U}{U_e} = C_o \left(\frac{y + a}{\delta}\right)^\gamma, \tag{2.18}$$

respectively. The multiplicative coefficients, C_i and C_o, as well as the exponent γ, are dependent on the Reynolds number $\delta^+ = \delta U_\tau / \nu$, and a^+ (= -16) represents a shift in origin for measuring y associated with the growth of the mesolayer region ($30 \leq y^+ \leq 300$). It should be noted that the origin shift, a, was not derived from the AIP, but rather introduced on the basis of addition arguments. Similar to Coles proposal, George and

Castillo (1997) added a wake term to obtain the following expression that describes the overlap region and outer region of the boundary layer

$$\frac{U}{U_e} = C_o\left(\frac{y+a}{\delta}\right) + (1-C_o)\frac{y}{\delta}\sin\left(B\frac{y}{\delta}\right). \tag{2.19}$$

As noted by George and Castillo (1997), their power-law has the following advantage over the log law: 1) the velocity profile will always exist even in the limit of infinite Reynolds number; 2) δ/δ^* and δ/θ will have a finite value asymptotically as opposed to the log-law which will blow up in the limit of infinite Reynolds number; and 3) the shape factor ($H = \delta^*/\theta$) will approach the finite value greater than unity. No experiments found the value of H less than 1.16 as apposed to the consequence of the log-law.

The power law discussion provided above was derived for zero-pressure gradient turbulent flow over a hydrodynamically smooth surface. It has, however, been used subsequently to process rough-wall mean velocity profile (Bergstrom *et al.*, 2001; Kotey *et al.*, 2003). The first attempt to modify the power law formulation for rough-wall application was made by Kotey *et al.* (2003). This was done on semi-empirical ground, and in their formulation, they re-write Eqn. 2.17 as

$$U_R^+ = \frac{C_i}{E}(y^+ + a^+)^{\gamma+\xi}, \tag{2.20}$$

where the sub-script R denotes rough-surface, E ($\geq$ 1) is a parameter introduced to reproduce the downward shift caused by roughness in the overlap region, and ξ ($\geq$ 0) accounts for the increase in wake parameter due to surface roughness.

Because the roughness shift ΔU^+ and k_s^+ are convenient parameters for describing roughness effects for engineering applications and modeling purposes, it is of interest to relate E to ΔU^+. In doing so, it should be noted that the power law is concave, and not a straight line, on a semi-log scale. However, if a common region of overlap is identified where both the power law and log-law are applicable for a rough surface, then we can write

$$\Delta U^+ = U^+ - U_R^+ \text{ or } \Delta U^+ = C_i\left(y^+ + a^+\right)^\gamma - \frac{C_i}{E}\left(y^+ + a^+\right)^{\gamma+\xi}. \tag{2.21}$$

In the above equation, the dimensionless mean velocity for smooth U^+ and rough U_R^+ surfaces should be determined at a particular y^+ value in the common overlap region as discussed above. Eqn. 2.21 can be re-arranged to give

$$E = \frac{C_i\left(y^+ + a^+\right)^{\gamma+\xi}}{C_i\left(y^+ + a^+\right)^\gamma - \Delta U^+}. \tag{2.22}$$

Note that for a smooth surface, $\xi = 0$ and $\Delta U^+ = 0$ so that $E = 1$. It should also be remembered that Eqn. 2.22 is valid only in the part of the overlap region where the log law and power law are valid simultaneously.

Seo (2003) also modified the original power law proposed by George and Castillo (1997) to account for the effects of surface roughness on the power law parameters C_o, C_i, and γ. The modified parameters are expressed in terms of k_s^+ as

$$\tilde{C}_o(\delta^+, k^+) = C_{o\infty}[1 + 0.00576(k^+)^{0.517}][1 + 0.283\exp(-0.00598\delta^+)], \tag{2.23}$$

$$\tilde{C}_i(\delta^+,k^+)=\left[\frac{C_{i\infty}}{1+0.03551(k^+)^{0.88647}}\right]\left(1+0.283\exp(-0.00598\delta^+)\right)\exp\left[\frac{-(1+\alpha)A}{(\ln\delta^+)^{\alpha}}\right], \quad (2.24)$$

and

$$\tilde{\gamma}(\delta^+,k^+)=\gamma_\infty+0.0065(k^+)^{0.60126}+\frac{\alpha A}{(\ln\delta^+)^{1+\alpha}}, \quad (2.25)$$

where $C_{0\infty} = 0.897$, $C_{i\infty} = 55$, $\gamma_\infty = 0.0362$, $A = 2.90$ and $\alpha = 0.46$. It should be noted that if $k_s^+ = 0$, Eqns. 2.23 – 2.25 reduce to the original expressions given by George and Castillo (1997).

2.1.6 Determination of Skin Friction

In any near-wall turbulence research, one of the most important parameters to determine is the friction velocity, and hence the skin friction. The various techniques applied in this research to obtain skin friction are discussed below.

2.1.6.1 The Clauser Plot / Log Law Approach

If the Reynolds number is high enough for a well-defined overlap region to exist, the skin friction is commonly determined by fitting the logarithmic profile (Eqn. 2.15) to the mean velocity data. This is the Clauser plot technique which is well established for smooth and rough surfaces. Since the log law parameters are assumed to be universal, the friction velocity (U_τ) is the only adjustable parameter in the log law. Once the friction velocity is obtained from this technique, the skin friction can be calculated using the following relationship

$$C_f = 2\left(\frac{U_\tau}{U_e}\right)^2. \tag{2.26}$$

However, some studies demonstrated that the Clauser technique for rough wall boundary layers may not be reliable. Perry *et al.* (1969) remarked that due to the additional roughness variables (i.e., the roughness shift, ΔU^+ and the virtual origin, ε), the Clauser plot technique for finding the wall shear stress would be inaccurate.

2.1.6.2 The Power Law Approach

The power law proposed by George and Castillo (1997) were also used to derive skin friction relations. This friction law proposed by George and Castillo (1997) is also power law in nature and is given by

$$\frac{U_\tau}{U_e} = \left(\frac{C_o}{C_i}\right)^{1/(1+\gamma)} \left(\frac{U_e \delta}{\nu}\right)^{-\gamma/(1+\gamma)} \tag{2.27}$$

or

$$C_f = 2\left(\frac{C_o}{C_i}\right)^{2/(1+\gamma)} \left(\frac{U_e \delta}{\nu}\right)^{-2\gamma/(1+\gamma)}. \tag{2.28}$$

Application of the power law to determine the friction velocity is more complicated than the log law. There are three adjustable parameters i.e., C_o, C_i and γ and these parameters are functions of Reynolds number and surface roughness. Appropriate selection of the power law parameters will yield a reasonable fit to the experimental data. Once the three parameters are known, skin friction can then be calculated using the above expression.

Note that the log law and the power law are profile matching techniques and their accuracy depends on how precisely the fitted parameters are chosen to describe the mean velocity profile.

2.1.6.3 Fringe Imaging Skin Friction Technique

As stated earlier, the fringe imaging skin friction (FISF) technique is used to perform independent skin friction measurements. The basic principle of the FISF technique is to measure the deformation of a thin film of oil when subjected to a shear stress on its top surface. A simple and convenient implementation of the FISF technique consists of illuminating the oil-film by a monochromatic light of wavelength λ, and recording the change in the generated interference pattern using a CCD camera for example. The distance Δs between the destructive interference bands of the interferogram is proportional to the thickness of the oil and in turn, proportional to the skin friction (by lubrication theory) for a near normal illumination, and zero pressure and shear stress gradients

$$C_f = \frac{\tau_w}{q_\infty} = \frac{2n_\circ \mu_\circ \Delta s}{q_\infty \lambda t} \tag{2.29}$$

where λ is the wavelength of the light source, μ_o is the absolute viscosity of the oil, n_o is the refractive index of the oil, t is the run time and q_∞ is the dynamic pressure. Zilliac (1999) developed a user-friendly software that integrates image acquisition and image processing, and this software is used in our study to determine the skin friction values.

2.2 Review of Previous Experiments

2.2.1 Reynolds Number Effects on Smooth Wall Turbulent Boundary Layers

When the surface is hydrodynamically smooth, the flow characteristics including the skin friction are primarily dependent on the flow Reynolds number. For this reason, numerous experiments have been conducted to study how the mean flow characteristics and turbulent quantities vary with Reynolds number (i.e., Purtell *et al.*, 1981; Degraaff, 1999; Österlund *et al.*, 1999). The smooth-wall experiments reported prior to 1994 were critically reviewed by Gad-el-Hak and Bandyopadhyay (1994).

The mean flow velocity in the streamwise direction is a relatively easy quantity to measure as consequence of modest probe resolution requirements. Such measurements can easily be found in almost every paper on wall-bounded flows (see, for example Preston and Sweeting 1944; Purtell *et al.*, 1981; Andreopoulos *et al.*, 1984; Kotey *et al.*, 2003). The results obtained from prior studies demonstrate that as Re_θ (= $U_e\theta/\nu$) increases, the mean-velocity profile becomes fuller and the shape factor, H, decreases accordingly. For example, at $\mathrm{Re}_\theta = 2000$, $H = 1.41$, and at $\mathrm{Re}_\theta = 10{,}000$, $H = 1.33$ (Gad-el-Hak and Bandyopadhyay 1994). The effect is even more pronounced at Reynolds numbers lower than 2000. In a laminar flat-plate, in contrast, viscosity is important across the entire layer and the shape factor is independent of Reynolds number.

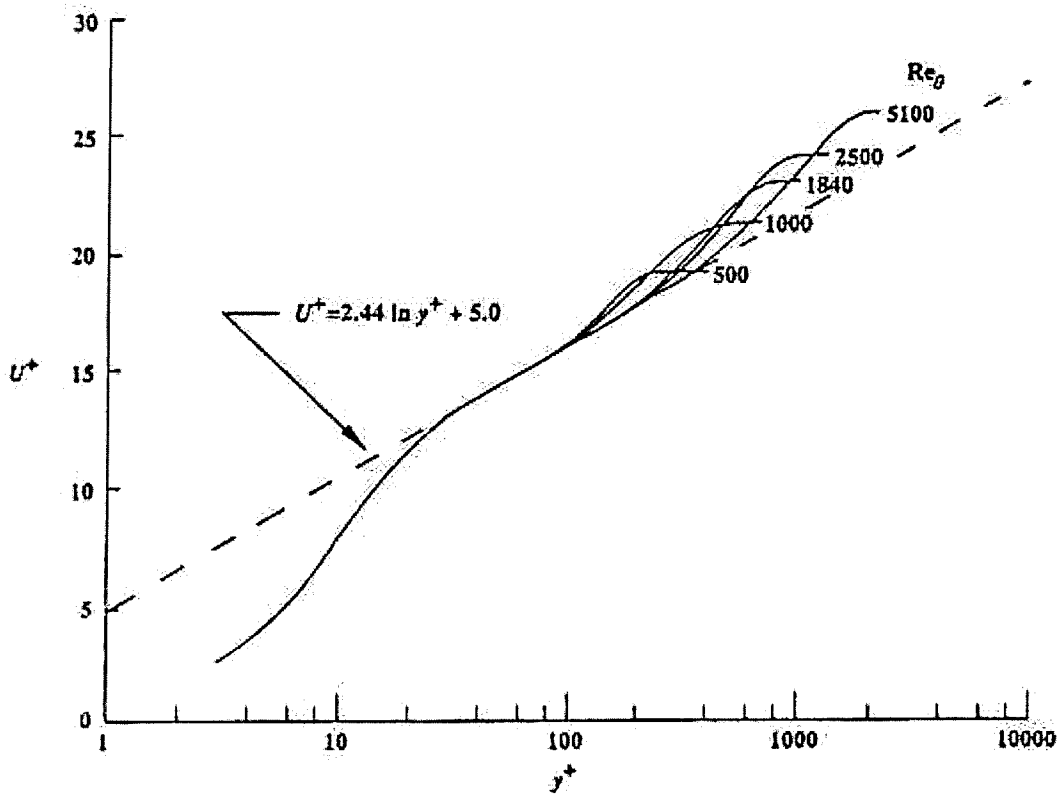

Figure 2-3: Comparison of mean-velocity profiles with logarithmic law at low Reynolds numbers (Purtell *et. al.*, 1981).

Available data appear to indicate that the wall-layer variables universally describe the streamwise mean velocity in the inner layer of smooth flat plates. Figure 2-3 illustrates this for boundary layers for a wide range of Reynolds numbers. The extent of log region, expressed in wall units, increases with Reynolds number but is a constant fraction of the boundary layer thickness. Furthermore, the viscous sublayer occupies progressively smaller portion of the boundary layer thickness as Re_θ increases. The low-Reynolds number boundary layer data of Purtell *et al.* (1981) in Figure 2-3 indicates the presence of the logarithmic region as low as 500. Gad-el-Hak and Bandyopadhyay (1994) find this rather surprising considering that at this Reynolds number a constant-stress region is virtually non-existent and the maximum Reynolds stress is substantially less than U_τ^2.

The single straight line in Figure 2-3 does not support Simpson's (1970; 1976) claim that the law-of-the-wall, especially κ, varies with Reynolds number, nor the assertion by Landweber (1953), Preston (1958) and Granville (1977) that the logarithmic region disappears all together at low Reynolds numbers. On the other hand, the supposedly universal values of κ, differ from investigator to investigator as shown earlier in Table 2.1. Unfortunately, lack of very high Reynolds number data makes the interpretations of the result very delicate; it is often hard to tell whether a finite asymptotic value exists.

Regardless of the Reynolds number the inner scaling seems to collapse wall-layer mean-flow data onto a single curve. However, the situation in the outer layer is quite different. The strength of wake (Π) is related to the maximum deviation ($\Delta U^+_{\max}$) of the profiles above the log law. It depends on the pressure gradient, the freestream turbulence and whether the flow is internal or external. The relationship is given by the following

$$\Delta U^+_{\max} = \frac{2\Pi}{\kappa}. \tag{2.30}$$

Figure 2-4 illustrates the change of maximum deviation of the mean velocity form the logarithmic law, $\Delta U^+_{\max}$, with Reynolds number (from Coles, 1962). The maximum deviation is expressed in wall units and the Reynolds number is based on momentum thickness and freestream velocity. Since, $\Delta U^+_{\max}$ is dependent on Re_θ and Π is related to $\Delta U^+_{\max}$ (Eqn 2.30), it is implied that Π is also dependent on Re_θ. It can be observed from Figure 2-4 that the $\Delta U^+_{\max}$ reaches a constant value for $\mathrm{Re}_\theta \geq 6{,}000$. Coles (1962) termed

the flow at this high Reynolds number "equilibrium," which led to the wide spread perception that the flow becomes independent of Reynolds number beyond this value. Coles' (1962) claim was based on the data available at that time but recent experiments in high Reynolds number contradict the claim, e.g., Degraaff (1999). Unfortunately, when the plot in Figure 2-4 is extended to larger values of Reynolds numbers, it becomes clear that the presumed asymptotic state is merely an illusion. As shown in Figure 2-5, ΔU^+_{max} starts decreasing again at about $Re_\theta > 15{,}000$, although very slowly compared to the rise rate for $Re_\theta < 6{,}000$.

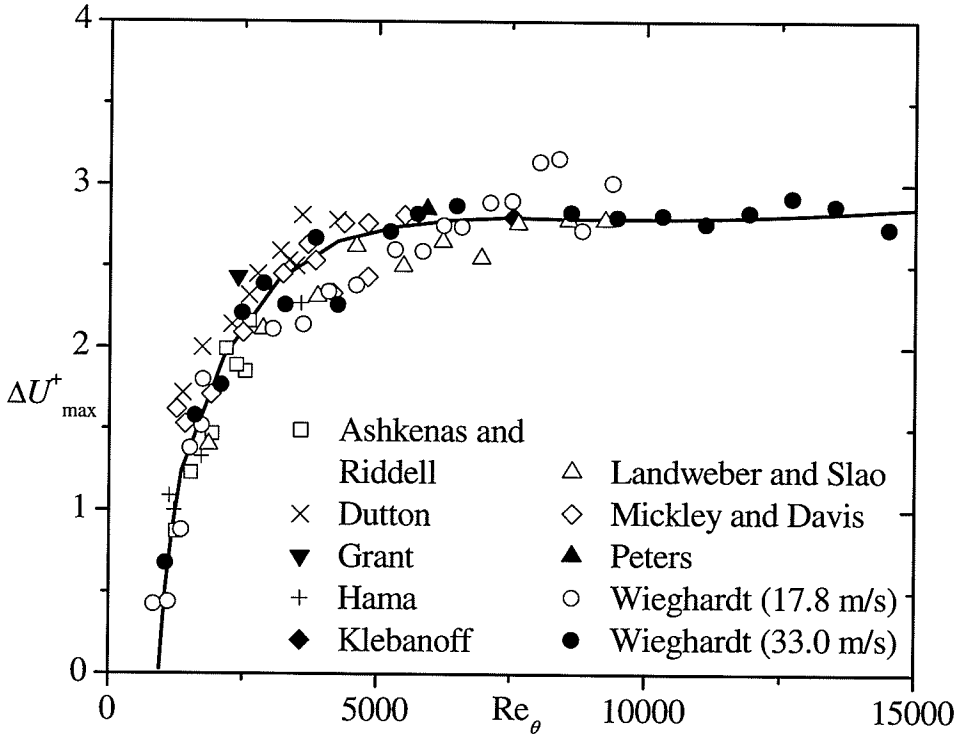

Figure 2-4: Coles' (1962) strength of the wake component in equilibrium turbulent boundary layer at low Reynolds numbers.

The rapid rise and the subsequent gradual fall of the ΔU^+_{max} with Re_θ appears to be genuine. This trend is consistent with the trends shown by several other researchers,

e.g., Fernholz and Finley (1996), Mabey (1979), Smith and Walker (1959) and Degraaff (1999). Degraaff (1999) suggests from his data that either the wake parameter asymptotes to a constant value at Reynolds numbers above the range of their study, or that it continues to decrease indefinitely. If it does continue to drop with increasing Reynolds number, then the law of the wake is not universal.

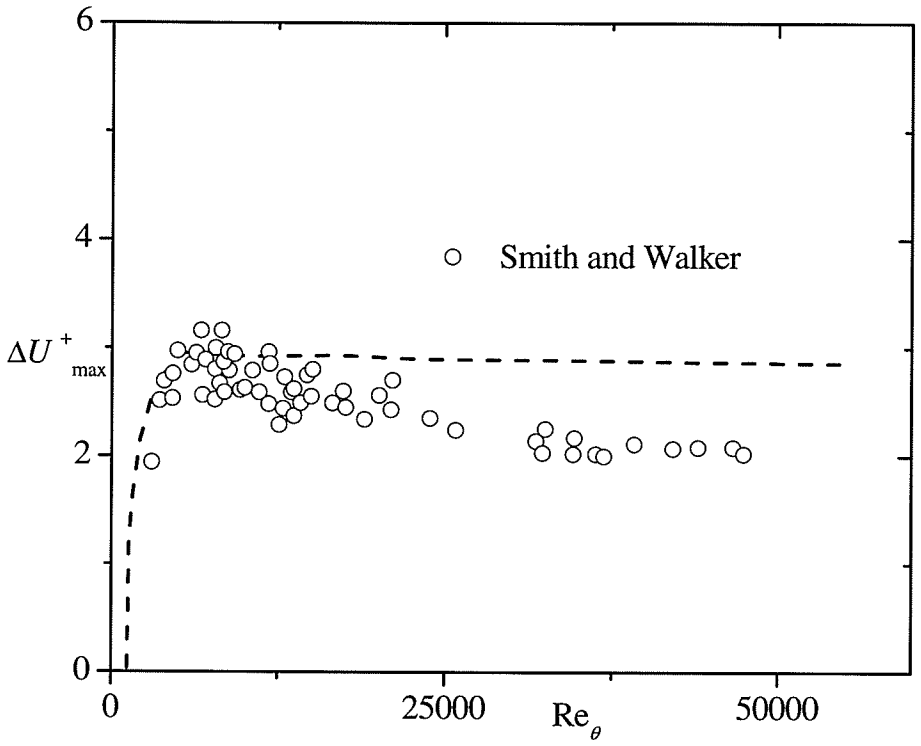

Figure 2-5: Reproduction of Coles' (1962) strength of the wake component at large Reynolds numbers (Gad-el-Hak and Bandyopadhyay, 1994).

2.2.2 Roughness Effects on Turbulent Boundary Layers

A significant amount of research has been dedicated to rough wall turbulent boundary layers, e.g., Furuya and Fujita (1967); Perry *et al.* (1969); Krogstad *et al.* (1992); Krogstad and Antonia (1999); Bergstrom (2002) as well as the review papers by Raupach *et al.* (1991) and Jiménez (2004). Most turbulence textbooks include material on roughness and the one by Schlichting (1968) is still a useful reference. Therefore, it is

helpful to review some of these papers to gain understanding of rough wall turbulent boundary layers.

Perry *et al.* (1969) experimentally studied rough wall turbulent boundary layer development over *k*- and *d*-typed roughness in zero pressure gradient and in fully rough regime. Perry *et al.* (1969) remarked that due to the additional roughness variables (i.e., the roughness shift, ΔU^+ and the virtual origin, ε), the Clauser plot technique for finding the wall shear stress would be inaccurate. The skin friction was determined by pressure tapping the roughness elements and measuring their form drag. Their experimental data revealed that the roughness function, ΔU^+, depends on a Reynolds number based on the friction velocity and on a length scale associated with the size of the roughness for a *k*-type roughness. On the other hand, the roughness function obtained for the *d*-type roughness did not show any dependency on roughness size but rather scaled on the Reynolds number based on an external length scale such as pipe diameter.

In their review, Raupach *et al.* (1991) considered theoretical and experimental knowledge of rough wall turbulent boundary layers drawn from both laboratory and atmospheric data. They specifically investigated the drag characteristics of rough surfaces as a function of the roughness geometry, the mean and turbulent velocity fields and the nature of organized motion in rough wall boundary layers. Finally, they advocated strong support for the hypothesis of wall similarity which states that at sufficiently high Reynolds numbers, rough wall and smooth wall boundary layers have the same turbulent structure above the roughness sublayer. That is, mean and turbulent

quantities for smooth and rough wall turbulent boundary layers, once normalized by appropriate scales, should collapse in the outer region.

An experimental study on surface roughness effects in canonical zero-pressure gradient turbulent boundary layers also in the fully rough regime was carried out by Krogstad and Antonia (1999). Their study was performed on stainless steel woven mesh screen and lateral rods that produce similar roughness shift ($\Delta U^+ = 11$, 10.5 respectively). The friction velocity on rough surfaces was obtained by using a velocity defect profile of the form

$$U_e^+ - U^+ = \frac{2\Pi}{\kappa}\left[w(1) - w\left(\frac{y}{\delta}\right)\right] - \frac{1}{\kappa}\ln\left(\frac{y}{\delta}\right). \tag{2.31}$$

Since, values of Π varied depending upon the types of roughness, they suggested that a fixed value of Π (i.e., $\Pi = 0.55$ used by Coles, 1956) may not yield optimum results. To account for Π dependence on surface roughness they employed a formulation which was originally proposed by Finley *et al.* (1966), namely,

$$w\left(\frac{y}{\delta}\right) = \frac{1}{2\Pi}\left[(1+6\Pi) - (1+4\Pi)\left(\frac{y}{\delta}\right)\right]\left(\frac{y}{\delta}\right)^2. \tag{2.32}$$

They found that apart from the roughness shift in the inner region, the strength of the wake is larger than on a smooth surface. The profiles of two different rough surfaces appear to be different in physical coordinates (U/U_e vs. y/δ) as shown in Figure 2-6. The plot using inner variables shows the shift from the smooth wall log law for the two rough surfaces, where the magnitude of the shift is the same for both type of roughness (see Figure 2-6). The velocity defect plot shows that the two rough surface profiles are very similar to smooth wall velocity profile in the outer layer, suggesting that surface

roughness effects are restricted to the inner wall layer which is misleading. However, Krogstad and Antonia (1999) argued that to characterize the roughness by simply inspecting the effect it has on the mean velocity profiles is inadequate.

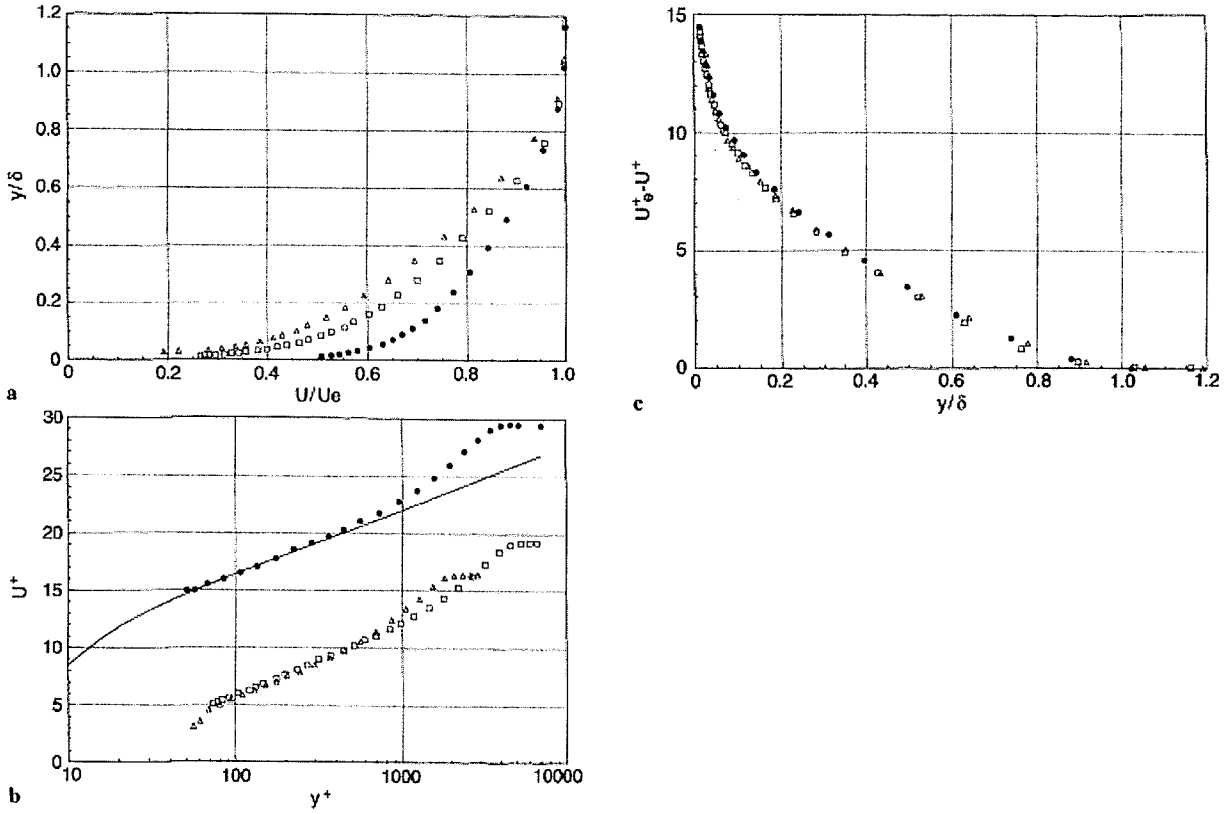

Figure 2-6: Mean Velocity profiles, a) outer variables; b) inner variables; c) velocity defect. (Δ) Rods; (∀) Mesh; (,) Smooth (Krogstad *et. al.*, 1999).

Bergstrom *et al.* (2002) carried out detailed experimental studies of turbulent boundary layer development over smooth and various different rough walls (including perforated steel plates, surface roughened by sand grains and woven steel wire mesh), in zero pressure gradient. The tests were conducted in hydrodynamically smooth and fully rough regime. Following Krogstad and Antonia (1999), the defect profile (Eqn. 2.31) along with the formulation (Eqn. 2.32) that allowed optimization of the Π values was

used to determine the friction velocity. The tests conducted on smooth surface yielded Π values of 0.55 and 0.54 at $Re_\theta = 5176$ and 7277, respectively. The values of Π ranged from 0.56 to 0.73 for rough surfaces, where wire mesh had the highest Π values. The Π values were distinctly higher for rough wall profiles compared to the value obtained for smooth wall. Their investigation also revealed that the type of surface roughness affects the mean velocity defect profile in the outer region of the turbulent boundary layer as well as determining the value of skin friction which negates the existence of a wall similarity hypothesis (also see Krogstad *et al.*, 1992). Also, irrespective of the surface geometry, roughness conditions with approximately same roughness shift, i.e., ΔU^+ have similar mean flow characteristics.

Kotey *et al.* (2003) conducted experiments on smooth and rough wall turbulent boundary layers in zero pressure gradient. The experiments were conducted on smooth and different rough surfaces (i.e., perforated steel plates, sand grain roughness and stainless steel wire mesh). They used log law and power law to obtain friction velocity on smooth and rough surfaces. However, they remarked that the power laws proposed by Barenblatt (1993) and Zagarola *et al.* (1997) failed to describe the rough wall data. Only the power law proposed by George and Castillo (1997) gave a reasonable fit to the rough wall experimental data. They concluded that the power law (proposed by George and Castillo, 1997) adequately describes the velocity profile of smooth and rough surfaces and provides accurate prediction of friction velocity. Also the power law describes the experimental data over a greater extent than log law in all the cases considered.

In summary, a great amount of research has taken place on rough wall boundary layers in fully rough regime. However, transitionally rough regimes are still poorly understood and not nearly researched enough when compared to smooth and fully rough regimes. One of the most recent rough wall turbulent boundary layer review is presented by Jiménez (2004). This paper reviews the experimental evidence and behavior of turbulent flows over rough walls in fully rough and transitionally rough regimes. According to Jiménez (2004) roughness has two effects in the transitional regime. In the first place it creates an extra form drag, which increases skin friction, but it also weakens the viscous generation cycle, which decreases it. The geometric offset in riblets is an example of the second effect, which is dominant in that case because the riblets, aligned with the mean flow, have little form drag. As k_s^+ increases, and the viscous cycle is completely destroyed, the savings from that effect saturate, and the form drag eventually takes over.

CHAPTER 3: EXPERIMENTAL SETUP AND PROCEDURE

This chapter describes the wind tunnel facility followed by the apparatus used for FISF technique. The instrumentation and measurement procedure for the mean velocity measurements are also presented.

3.1 The Wind Tunnel Facility

The experiments were performed in the high-speed test section (HSTS) of a single-return wind tunnel at the University of Saskatchewan. The schematic of the wind tunnel can be seen in Figure 3-1. The test section was 1.12 m x 0.91 m in cross-section, and approximately 2.00 m long. The flow entered the high-speed test section from the low-speed test section via a 7:1 contraction. The side-walls are made of Plexiglas to facilitate visual inspection of probe positions during experiments. At the bottom of this section is an elevated ground plane where test models can be mounted. Also housed in the HSTS is a traversing wing that provides a means of positioning measurement equipment. There are vents or "breathers" at the rear of the HSTS to prevent static pressure drift as the air heats up during a test. The velocity range that can be attained in this section is 5-60m/s.

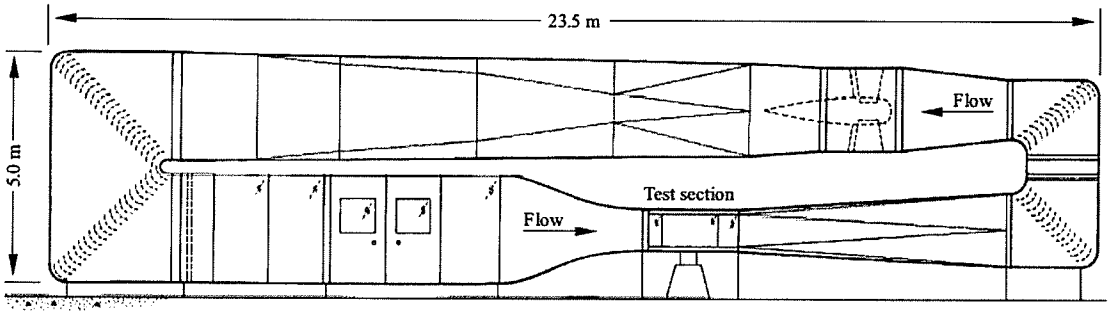

Figure 3-1: University of Saskatchewan Low-Speed Wind Tunnel.

3.2 The Ground Plane

The skin friction and velocity measurements were made on a Medium Density Fiber (MDF) board, and not on the floor of the wind tunnel. The MDF board was 1.67 m long, 1.16 m wide and 25 mm thick, and was mounted on the floor of the wind tunnel. Streamlined risers were used to maintain 40 mm spacing between the bottom of the MDF board and the floor of the wind tunnel. The large-scale deviation of the surface was less than ± 0.5 mm from the horizontal plane. The leading edge of the board was carefully rounded to an elliptical profile to avoid flow separation and to improve flow quality. To facilitate a rapid development of a turbulent boundary layer, the flow was tripped using a 36 grit sand paper. The trip was 4 inches long, located at the leading edge and across the entire width of the MDF board.

3.3 The FISF System

A schematic of the FISF system used in this study is shown in Figure 3-2. The system consists of an optical and an imaging system, a model surface, a candidate oil and software for image capture and analysis. The imaging system consists of a black and white ½" format CCD camera (Sony XCD-X700), a macro zoom camera lens (Computar MLH–10X Macro Zoom) and a green filter (Filter Dichroic Green, NT52-535 50x2 mm). The resolution of the camera was 1024x768 pixels. Images taken from the camera were stored as *.bmp format on a laptop computer using a Firewire card (IEEE1394 Cardbus Controller). The light source used in our experiments was a fluorescent tube light (SLi Lighting, F17T8/841, 17 Watts) with a green tube shell. The interference green filter was placed in front of the camera so that only the spectral components near the center

wavelength of the filter was transmitted resulting in a quasi-monochromatic fringe pattern. The oil used was silicone oil (Dow Corning 200® 100cs fluid). Silicone oil was chosen because its viscosity is relatively insensitive to temperature; it is also optically transparent and relatively easy to clean. The refractive index of the silicone oil is 1.4032 @ 25 °C. A 50/50 beam splitter was used to reflect 50% of the incident energy, absorb a relatively small portion, and transmit the remaining energy. Figure 3-2 also shows an opal diffusing sheet placed between the light source and CCD camera. The purpose of the diffusing element was to create an "extended" light source (as opposed to a distant point light source which generates parallel rays). This was necessary because interference fringes can be seen or imaged only if there is a small variation in the incidence angle of the light hitting the oil surface (Zilliac, 1996). Since the MDF board does not have the high optical quality required to enhance the fringes produced, black Monokote® was carefully taped on the MDF board to create the model test surface. The black Monokote® was chosen because it has very smooth and high-gloss surface. It is also puncture and scratch resistant, and has been successfully used in prior FISF experiments (Bourassa *et al.*, 2000).

To perform skin friction measurement, a drop or line of the silicone oil was placed near the desired measurement downstream location x on the black Monokote® in the wind tunnel. The airflow was turned on and the oil was allowed to spread. After several minutes, typically 5 to 8 minutes, the oil forms a wedge (in cross section) with a nearly linear profile. The flow was then turned off, and the imaging system discussed earlier was used to capture the fringes formed on the model surface. A linear scale was

also placed beside the fringes to calibrate the fringe spacing. The experiments were performed at four different freestream velocities (U_e = 15, 22, 35 and 42 m/s) and at several downstream location. The software (Zilliac, 1999) determines the fringe intensity distribution by utilizing the fringe fronts starting upstream of the oil flow and extending downstream of the second fringe. Prior to image analysis, the digitized images were enhanced using Photo Impression.

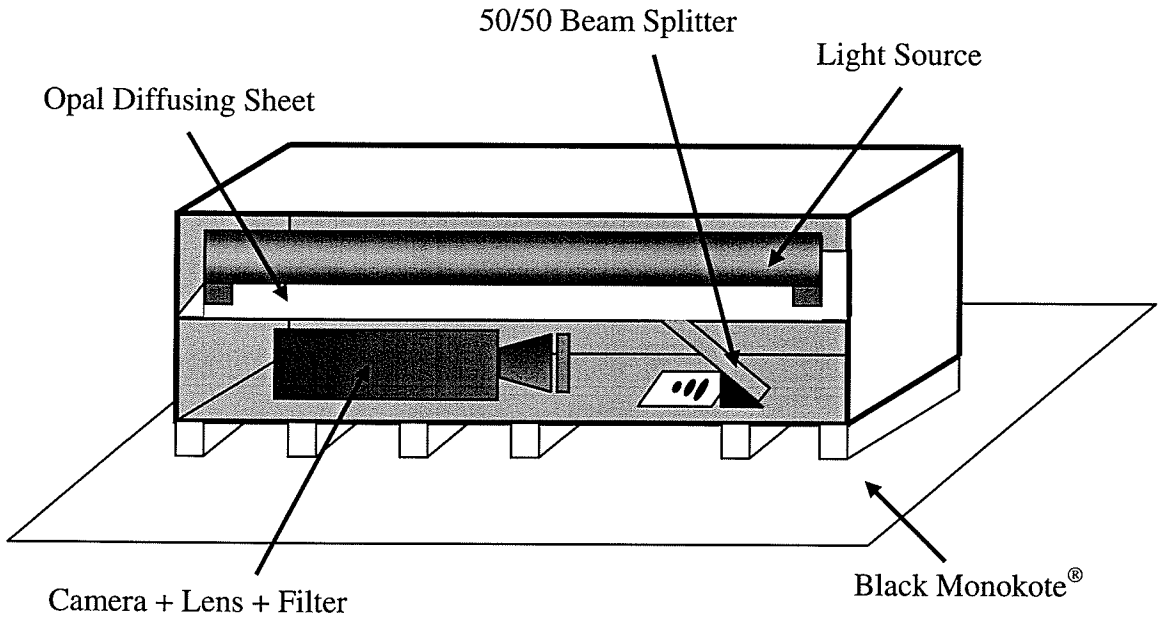

Figure 3-2: A schematic of the fringe imaging skin friction (FISF) optical and imaging system.

3.3.1 Fringe Analysis Using PC Application

CXWIN4G is a PC application developed by Dr. Zilliac, at NASA Ames, to determine the skin friction at various points on surface. It is specifically designed to process the interferograms that are imaged as of the FISF technique. The images are first calibrated, using a one-camera photogrammetry approach. This process relates the image plane to the physical coordinates. Then the application applies a nonlinear regression model,

which uses a quasi-Newton method, to accurately determine the fringe spacing from interferometric intensity records. The skin friction is found through application of the simple expression (i.e., Eqn. 2.29) that makes use of lubrication theory to relate fringe spacing to skin friction.

Analyzing the fringes formed on the model surface requires: 1) a digitized grey scale image (TIF format) of an FISF interferogram (image should have reference marks for calibration); 2) the wavelength of the light (542 nm) that created the interferogram; 3) the viscosity of the oil (100cs) that was used; 4) the dynamic freestream pressure (in inches of H_2O); 5) the temperature of the flow (in $°F$); and 6) the duration (in sec.) that the oil was exposed to the flow is required. The skin friction magnitude can then be obtained from the software with minimal effort. Detailed procedure of analyzing an image using CXWIN4G can be seen in Appendix A.

3.4 The Roughness Elements

The rough surfaces were made from sand paper of varying grit, steel perforated plate of varying plate thickness and hole diameter, and a stainless steel woven wire mesh of varying wire diameter and openness ratio. The specific roughness elements are as follows: (i) Sand paper: (a) 120-grit (SP-1), (b) 80-grit (SP-2), (c) 60-grit (SP-3) and (d) 40-grit (SP-4); (ii) Perforated plate: (a) thickness = 0.76 mm, hole diameter = 1.2 mm, openness ratio = 22% (PF-1); (b) thickness = 0.90 mm, hole diameter = 1.6 mm, openness ratio = 41% (PF-2); (c) thickness = 0.90 mm, hole diameter = 2.0 mm, openness ratio = 45% (PF-3); (iii) Woven wire mesh: (a) diameter = 0.36 mm, openness

ratio = 44% (WM-1); (b) diameter = 0.58 mm, openness ratio = 30%; (c) diameter = 1.04 mm, openness ratio = 35%.

3.5 Velocity Measurement

Detailed mean velocity profiles across the boundary layer were obtained using a Pitot probe with outer diameter of 0.60 mm. To facilitate comparison between the smooth-wall skin friction values determined from the velocity profiles (i.e., log law and power law) and the FISF technique, the smooth-wall velocity measurements were also obtained on the black Monokote®. The trip device used in the FISF experiments was also used during the mean velocity measurements. This was necessary to maintain similar upstream conditions and the development of the boundary layer in both experiments. Velocity measurements were obtained by taking 5000 samples of the dynamic pressure at a sampling frequency of 1000 Hz. A 0.2 mm y-step was used close to the wall, 0.5 mm y-step in the intermediate region, and 1.0 mm y-step away from the wall. The small y-increments close to the wall were necessary to obtain adequate data points in the overlap region for an accurate determination of the friction velocity from the Clauser chart technique. Corrections were applied to the Pitot tube data following MacMillan (1956). The nominal freestream turbulence intensity and pressure gradient were, respectively, 0.6% and -10 Pa/m. The non-uniformity of the freestream velocity profile was 0.5% or less.

The smooth-wall velocity measurements were obtained at freestream velocities U_e similar to those used for the FISF measurements, and at several streamwise locations, x.

However, the data reported here were obtained at x = 1000 and 1200 mm from the boundary layer trip. All the rough-wall experiments were made at $U_e \approx 25$ m/s. A summary of important test parameters is given in Table 3-1, where, U_e is the freestream velocity, δ is the boundary layer thickness defined as the location above the surface at which the local mean velocity is 99% of the freestream value, δ^* is the displacement thickness, θ is the momentum thickness, H is the shape parameter, $\mathrm{Re}_\theta = U_e\theta/\nu$, Π is Coles wake parameter, ΔU^+ and k_s^+ are, respectively, the roughness shift and equivalent sand grain parameter. The notations -1, -2, -3, -4 denote increasing Reynolds number for the smooth surface, and increasing roughness effects (ΔU^+) for the rough surfaces. It is clear from Table 3-1 that the Π values for the rough surfaces are, on the average, higher than the corresponding smooth-wall values. Relatively higher Π values were obtained in some earlier studies (Krogstad *et al.*, 1992; Tachie *et al.*, 2000; Bergstrom *et al.*, 2002), and are indication of roughness effects extending into the outer region of the mean flow. On the basis of k_s^+ values summarized in Table 3-1 and roughness classification according to White (1991), PF-1, PF-2, SP-1, SP-2 and SP-3 are in the transitionally rough regime while PF-3, SP-4, WM-1, WM-2 and WM-3 are in the fully rough regime.

Table 3-1: Summary of test conditions and boundary layer parameters.

Test	x (mm)	U_e (m/s)	δ (mm)	δ^* (mm)	θ (mm)	Re_θ	H	Π	ΔU^+	k_s^+
SM-1	1000	15.18	31.6	4.52	3.36	2750	1.34	0.31	--	--
	1200	15.18	34.0	4.99	3.72	3030	1.34	0.38	--	--
SM-2	1000	22.67	31.5	4.58	3.40	4160	1.35	0.48	--	--
	1200	22.65	33.5	4.91	3.67	4460	1.34	0.43	--	--
SM-3	1000	35.29	28.2	3.79	2.86	5390	1.33	0.36	--	--
	1200	35.30	30.0	4.02	3.04	5710	1.32	0.37	--	--
SM-4	1000	42.02	28.0	3.82	2.87	6490	1.33	0.42	--	--
	1200	42.15	29.8	4.02	3.04	6780	1.32	0.40	--	--
PF-1	1200	25.46	33.3	5.32	3.82	5830	1.39	0.56	2.0	14
PF-2	1200	25.38	32.5	5.75	4.03	6090	1.43	0.54	4.3	30
PF-3	1200	25.19	33.7	6.88	4.51	6770	1.53	0.56	7.4	88
SP-1	1200	25.98	31.0	5.30	3.77	5770	1.41	0.48	3.1	20
SP-2	1200	25.03	32.4	5.80	4.00	5990	1.45	0.52	4.9	40
SP-3	1200	25.23	33.4	6.45	4.35	6560	1.48	0.64	5.9	53
SP-4	1200	25.55	35.6	6.97	4.62	6840	1.51	0.54	7.7	100
WM-1	1200	25.57	35.8	7.45	4.87	7250	1.53	0.65	7.7	97
WM-2	1200	25.73	35.3	7.65	4.90	7540	1.56	0.63	8.6	143
WM-3	1200	25.62	36.6	8.23	5.02	7840	1.64	0.69	9.9	248

3.6 Measurement Uncertainties

The measurement uncertainties were estimated at 95% confidence limits and typical values are summarized in Table 3-2 as follows:

Table 3-2: Summary of measurement uncertainties.

Parameter	Uncertainty Estimate (Smooth Wall)	Uncertainty Estimate (Rough Wall)
Wall-normal position (y) (near wall)	± 2%	± 10%
Local velocity (U) (near wall)	± 2%	± 2%
Local velocity (U) (away from wall)	± 1%	± 1%
Boundary layer thickness (δ)	± 5%	± 5%
Friction velocity (U_τ)	± 3%	± 3.5%
Freestream velocity (U_e)	± 0.5%	± 0.5%

Skin friction values obtained form FISF technique were estimated to have an uncertainty of ± 5%. The sample uncertainty analysis can be seen in the Appendix B.

CHAPTER 4: RESULTS AND DISCUSSION

The results and discussion of the present study are reported in this chapter. The mean velocity defect profiles are plotted using three different types of scaling (U_e, U_τ and $U_e\delta^*/\delta$). The log law and power law are applied to both smooth and rough surfaces to determine the friction velocity, U_τ. The skin friction values obtained from the log law and power law are compared to the values obtained from FISF technique. Power law parameters for smooth and rough surfaces are compared to the corresponding values obtained from the correlations proposed by George and Castillo (1997) for smooth surface and Seo (2003) for rough surfaces.

4.1 Mean Velocity Profiles in Outer Coordinates

The mean velocity profiles are plotted at various Reynolds number in Figure 4-1 using outer coordinates (U_e, δ). Figure 4-1a shows the profiles over a smooth surface at various Reynolds number obtained at x = 1000 mm for all the test conditions, and profiles obtained at x = 1200 mm are shown in Figure 4-1b. The error bars at selected data points in this and subsequent figures represent measurements uncertainty at 95 percent confidence interval. The figure demonstrates a slight Reynolds number effect.

The data obtained over the perforated plate, sand paper and wire mesh are compared with a reference smooth wall data (SM-2 at x = 1200 mm) in Figure. 4-2a, 4-2b and 4-2c, and Figure 4-2d compares velocity profiles obtained on various surfaces at similar freestream velocity. These figures demonstrate that the rough-wall profiles deviate from the smooth-

data over most of the boundary layer. The amount of deviation of the rough-wall data from the smooth wall data increases with increasing roughness effects, that is, as the friction drag increases. This observation is consistent with those made in prior experiments (Krogstad *et al.*, 1992 and Bergstrom *et al.*, 2002). Figure 4-2d clearly demonstrates a lack of collapse among profiles obtained on different surfaces.

4.2 Mean Velocity Defect Profiles

The mean velocity defect profiles are plotted in Figure 4-3 and Figure 4-4 using the scaling proposed by the classical theory (U_τ, δ). It is clear that the profiles obtained on a geometrically similar surface collapse reasonably well. That is, all the smooth profiles collapse in to a single curve (Figure 4-3a and 4-3b), the perforated plate and sand paper profiles also collapse well (Figure 4-4a and 4-4b). On the other hand, Figure 4-4c shows a lack of collapse between the smooth and wire mesh profiles especially in the region $y/\delta < 0.3$. Once again, Figure 4-4d clearly demonstrate a lack of collapse among profiles obtained on different surfaces.

In their power law formulation, George and Castillo (1997) proposed the freestream velocity U_e as the proper outer velocity scale. When the defect profiles are plotted in this format (Figure 4-5 and Figure 4-6), the defect profiles exhibit significant Reynolds number and roughness effects. That is, profiles obtained at various Reynolds number and on geometrically similar surfaces do not collapse into a single curve. The lack of collapse among individual profiles is much more pronounced than observed in Figure 4-3 and Figure 4-4, where U_τ was used to scale the mean velocity.

The mean velocity defect profiles are re-plotted in Figure 4-7 for smooth surfaces and Figure 4-8 for rough surfaces using the scaling $U_e\delta^*/\delta$, proposed by Zagarola and Smits (1998) for fully developed pipe flow, and subsequently used by Castillo and Walker (2002) and Akinlade *et al.* (2004) to collapse smooth and rough wall data in zero-pressure gradient turbulent boundary layers. Unlike previous two velocity scales (i.e., U_τ in Figure 4-3 and 4-4, and U_e in Figure 4-5 and 4-6), Figure 4-7 demonstrates that $U_e\delta^*/\delta$ collapses the smooth wall profiles at various Reynolds numbers, and profiles obtained over geometrically different roughness elements (Figure 4-8) remarkably well.

4.3 Mean Velocity in Inner Coordinate: Log Law and Power Law

As indicated in Chapter 2, the overlap region of the mean velocity profile can be modeled using the classical theory (log law) or the power law. That is, U_τ can be determined by fitting the log law or power law to the experimental data. For the log law, the friction velocity is the only adjustable parameter. For the rough-wall data, the virtual origin ε was estimated as 25% of the physical size of the roughness element and subsequently varied to achieve a good agreement between the velocity data and the log law in the near-wall region. The final or optimal value of ε was found, in some cases, to be quite different from the original estimate. This may be partly due to uncertainty associated with the exact location of the Pitot-tube with respect to the top-plane of the roughness elements. For both the smooth and rough-wall data, a decision was made to fit the log-law to data in the range $30 < y^+ < 0.2\,\delta^+$. The U_τ values obtained by applying the log law to the smooth and rough surfaces are summarized in Table 4-1.

As for power law, there are three adjustable parameters (C_o, C_i and γ) in addition to U_τ, and these parameters are functions of Reynolds number and surface roughness. The power law in the outer coordinate does not contain U_τ, we first fit Eqn. 2.19 to the experimental data to determine C_o and γ. The use of Eqn. 2.19 (rather than Eqn. 2.18) ensures that many data points (up to $y = \delta$) are used in the profile matching so that any uncertainty in ε should have only marginal effect on C_o and γ values. For both the smooth and rough surfaces, the value of $B = 2.03$ recommended by George and Castillo (1997) was used in Eqn. 2.19. With the value of γ determined from Eqn. 2.19, as explained above, U_τ and C_i were then be determined according to Eqn. 2.17.

Figure 4-9 and Figure 4-10 show the experimental data (symbols) and corresponding power law fits (solid lines) for the smooth and rough surfaces in outer coordinates respectively. The dash-dotted lines on the rough data (Figure 4-10) represent the power law fit to a reference smooth wall data (SM-2). The agreement between the power law and the experimental data is good for both the smooth and rough surfaces. The values of C_o and γ used to produce the fits are summarized in Table 4-1. The values of C_o vary only minimally with Reynolds number and surface conditions. On the hand, the values of γ for the rough surfaces are significantly higher than for the smooth surface. Higher values of γ were also noted by Kotey *et al.* (2003) and Bergstrom *et al.* (2001), and are consistent with the fact that rough-wall profiles are more concave than for smooth, and also consistent with the higher Π values obtained for the rough surfaces compared with the smooth data (Table 3-1).

Figure 4-11 and Figure 4-12 shows the velocity profiles in inner coordinates on a semi-log scale. Both power law (solid lines) and log law (dotted lines) are shown in each figure. A reference smooth-wall data set (SM-2) is denoted by dash-dotted lines on each of the rough data. The vertical lines on the rough data denote the level of the roughness shift (ΔU^+) from the smooth-wall log profile. It is clear from the figures that the power law covers significantly wider range of data compared with log law. The C_i values for both smooth and rough surfaces are summarized in Table 4-1. The values of C_i for the rough surfaces are generally lower for the rough surfaces than for smooth surface, as expected. For a given surface, the C_i value decreases as roughness effect (ΔU^+) increases. The U_τ values determined from Eqn. 2.27 and values of C_o, C_i and γ obtained from the profile matching are summarized in Table 4-1. The U_τ values obtained by using the power law are comparable to those obtained from the log law, Table 4-1, the percentage difference being 2.5% or less in all cases except for Test PF-3 (with a 4.5% difference).

4.4 Comparison of Power Law Parameters

As shown in Table 4-1, the values of C_o for the smooth surface are nearly independent of Reynolds number, C_i increases with increasing Reynolds number, and γ decreases weakly as Reynolds number increases. The C_i and γ values reported in Table 4-1 are similar to those obtained by Bergstrom *et al.* (2001) and Kotey *et al.* (2003) at similar Reynolds numbers; however, the present C_o values are about 4% higher. It should also be pointed out that the present smooth-wall parameters are comparable to those obtained from the experimental data sets used by George and Castillo (1997) to develop their correlation.

The power law parameters predicted from the smooth-wall correlations developed by George and Castillo (1997) and the rough-wall correlations developed by Seo (2003), i.e., Eqns. 2.23 - 2.25, are summarized in Table 4-2. In applying Eqns. 2.23 - 2.25, the k_s^+ values summarized in Table 3-1 were used. Also shown in Table 4-2 are the percent differences between our present (experimental) values and predicted values. For the smooth surface, the present C_o values are 8% or less higher, C_i values are 15% or less lower, and γ values are 23% or less higher. For the rough surfaces, the maximum differences between the present and predicted C_o values is 5%, 17% for C_i, and 16% for γ. These differences for the rough surfaces are comparable to those noted for the smooth surface. They are also comparable to the scatter of the experimental data used to develop the correlations (Seo, 2003).

The present results are also compared with the formulation of Kotey *et al.* (2003). In order to relate E to ΔU^+ (Eqn. 2.22), we chose reference smooth-wall values of C_i = 9.2 and γ = 0.13. These (C_i and γ) values correspond to SM-4, the maximum smooth-wall Reynolds number obtained in the present study. As can be seen from Figure 4-11 and Figure 4-12, the log law and power law overlap with the rough-wall data in the range $50 \leq y^+ \leq 350$, and so preliminary computations were performed using $(y^+ + a^+) = 100$, 200 and 300. It was observed that the deviations among the values of E computed from the various $(y^+ + a^+)$-values are less than 2%. For consistency, though, all the results reported (Table 4-2) were computed using $(y^+ + a^+) = 300$. Table 4-3 compares the values of E computed from Eqn. 2.22 to the experimental data. The experimental values of E were obtained from $C_i/C_{i,R}$, (with C_i = 9.2, and $C_{i,R}$ is the corresponding value for a

rough surface as summarized in Table 4-1). The differences between the computed and experimental values of E are less than 2%. The variation of E with ΔU^+ for the present and prior (Kotey *et al.*, 2003) experiments is shown in Figure 4-13. As can be seen, the values of E increase as ΔU^+ increases. This is to be expected because a higher roughness shift corresponds to a lower value of C_i (or $C_{i,R}$) for a rough surface. All the data shown in Figure 4-13, irrespective of the specific surface roughness geometry and roughness regime, can well be represented by the following relation

$$E = 3.07 \exp\left(\Delta U^+ / 12.47\right) - 2.5 . \tag{4.1}$$

4.5 Comparison among Skin Friction Coefficient Values

The values of the skin friction obtained in the present work using the FISF technique, and from the log law and power law are compared in Figure 4-14. The skin friction correlation developed by Österlund *et al.* (1999) based on their FISF measurements and a correlation developed from $1/7^{th}$ power law are also shown for comparison. The agreement among skin friction values determined in the present work and prior correlations are good. Specifically, the skin friction values obtained from the present FISF technique show a maximum deviation of 4% when compared to Österlund FISF correlation. The 4 percent deviation is within measurement uncertainty. The good agreement between the present power law values and the $1/7^{th}$ power law correlation is not surprising because our γ values are not significantly different from $1/7$, and the power law coefficients C_i are similar to typical values used for the traditional $1/7^{th}$ power law approximation for turbulent boundary layers. The close agreement between the log-

law and power law values suggest that, irrespective of the underlying theoretical arguments, both theories can give reasonable estimate of the skin friction characteristics.

Table 4-1: Summary of power law parameters and friction velocity.

							Power Law	Log Law
Test	x (mm)	Re_θ	δ^+	C_i	C_o	γ	U_τ (m/s)	U_τ (m/s)
SM-1	1000	2750	1290	8.76	0.95	0.138	0.613	0.628
	1200	3030	1400	8.83	0.96	0.136	0.616	0.619
SM-2	1000	4160	1830	8.92	0.95	0.136	0.874	0.877
	1200	4460	1940	9.00	0.95	0.134	0.866	0.878
SM-3	1000	5390	2490	9.11	0.96	0.133	1.326	1.353
	1200	5710	2640	9.20	0.97	0.130	1.322	1.345
SM-4	1000	6490	2940	9.15	0.97	0.130	1.573	1.574
	1200	6780	3070	9.20	0.97	0.130	1.548	1.575
PF-1	1200	5830	2020	6.93	0.96	0.163	1.016	1.038
PF-2	1200	6090	2150	5.30	0.96	0.185	1.111	1.139
PF-3	1200	6770	2440	3.24	0.96	0.229	1.219	1.277
SP-1	1200	5770	2000	6.26	0.96	0.170	1.095	1.125
SP-2	1200	5990	2190	4.90	0.97	0.192	1.132	1.157
SP-3	1200	6560	2460	4.15	0.98	0.206	1.228	1.200
SP-4	1200	6840	2670	3.05	0.99	0.235	1.300	1.320
WM-1	1200	7250	2630	3.05	0.96	0.235	1.266	1.279
WM-2	1200	7540	2790	2.45	0.99	0.260	1.321	1.345
WM-3	1200	7840	3100	1.76	1.00	0.292	1.390	1.408

Table 4-2: Comparison between experimental and predicted values of the power law parameters.

Test	C_i'	ΔC_i (%)	C_o'	ΔC_o (%)	γ'	$\Delta\gamma$(%)
SM-1	9.93	11.80	0.90	5.57	0.111	19.21
	10.02	11.88	0.90	6.56	0.110	18.93
SM-2	10.31	13.45	0.90	5.58	0.106	21.74
	10.37	13.20	0.90	5.58	0.106	21.74
SM-3	10.63	14.28	0.90	6.56	0.102	22.98
	10.69	13.92	0.90	7.14	0.102	21.76
SM-4	10.80	15.25	0.90	7.72	0.100	22.75
	10.84	15.13	0.90	7.72	0.100	23.13
PF-1	7.61	9.78	0.92	4.46	0.137	16.03
PF-2	6.08	14.64	0.93	3.44	0.155	16.47
PF-3	3.69	13.96	0.95	1.13	0.198	13.37
SP-1	6.91	10.36	0.92	4.03	0.145	14.94
SP-2	5.43	10.72	0.93	3.94	0.164	14.70
SP-3	4.83	17.05	0.94	4.36	0.206	16.08
SP-4	3.45	12.97	0.95	3.75	0.205	12.68
WM-1	3.51	15.10	0.95	0.84	0.203	13.45
WM-2	2.76	12.85	0.96	2.61	0.229	11.77
WM-3	1.90	7.77	0.99	1.36	0.279	4.51

Table 4-3: Summary of the power law parameters for rough surfaces.

Test	ΔU^+	C_i	ξ	E (Eqn. 2.22)	E^* (= $C_i/C_{i,R}$)	$\Delta E(\%)$
PF-1	2.0	6.93	0.033	1.35	1.33	1.4
PF-2	4.3	5.30	0.055	1.76	1.74	1.4
PF-3	7.4	3.24	0.099	2.85	2.84	0.4
SP-1	3.1	6.26	0.040	1.50	1.47	1.8
SP-2	4.9	4.90	0.062	1.91	1.88	1.6
SP-3	5.9	4.15	0.076	2.22	2.22	0.0
SP-4	7.7	3.05	0.105	3.03	3.02	0.3
WM-1	7.7	3.05	0.105	3.03	3.02	0.3
WM-2	8.6	2.45	0.130	3.78	3.76	0.8
WM-3	10.0	1.76	0.162	5.20	5.23	0.6

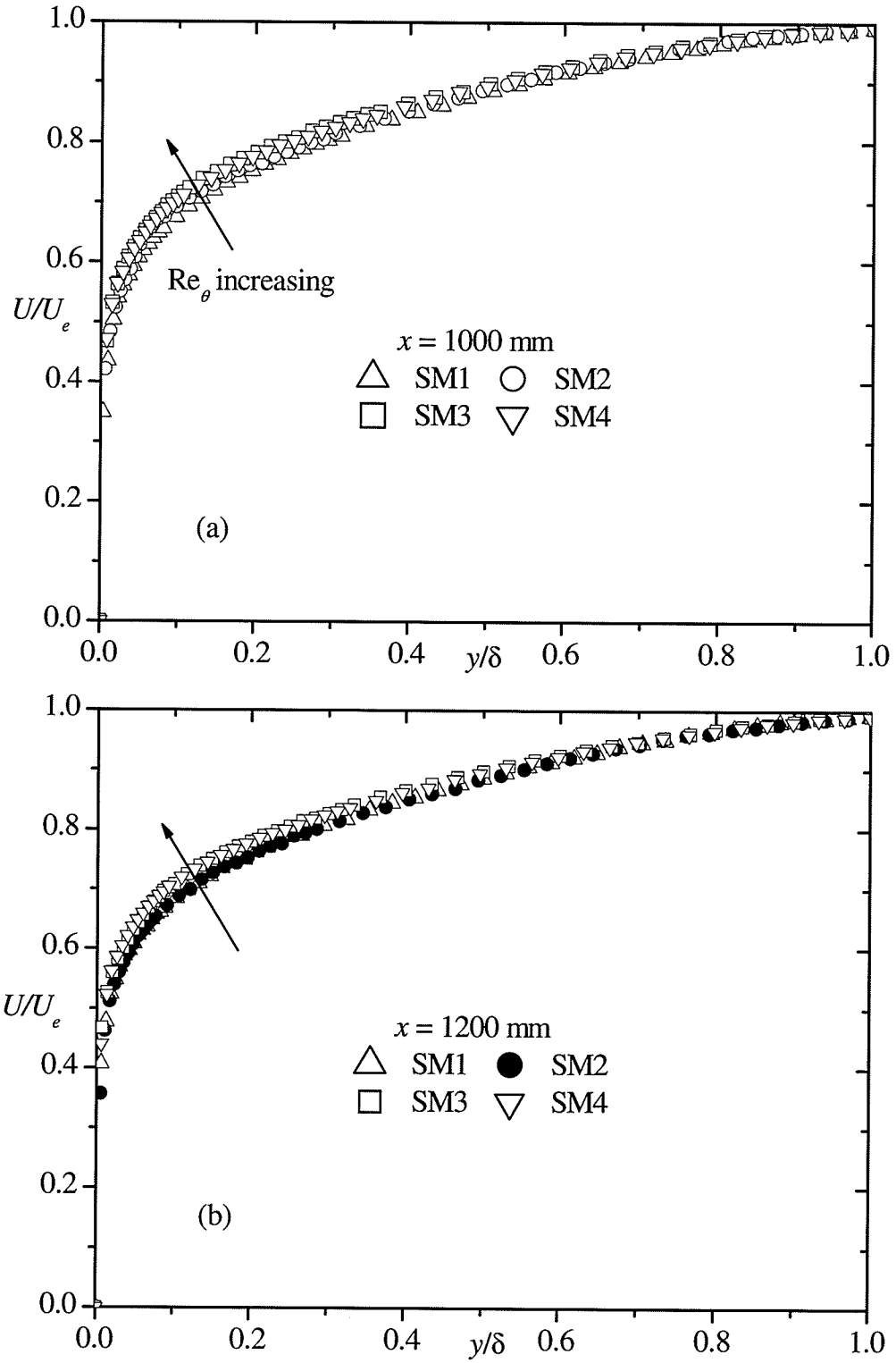

Figure 4-1: Mean velocity profiles at various Reynolds numbers using outer coordinates.

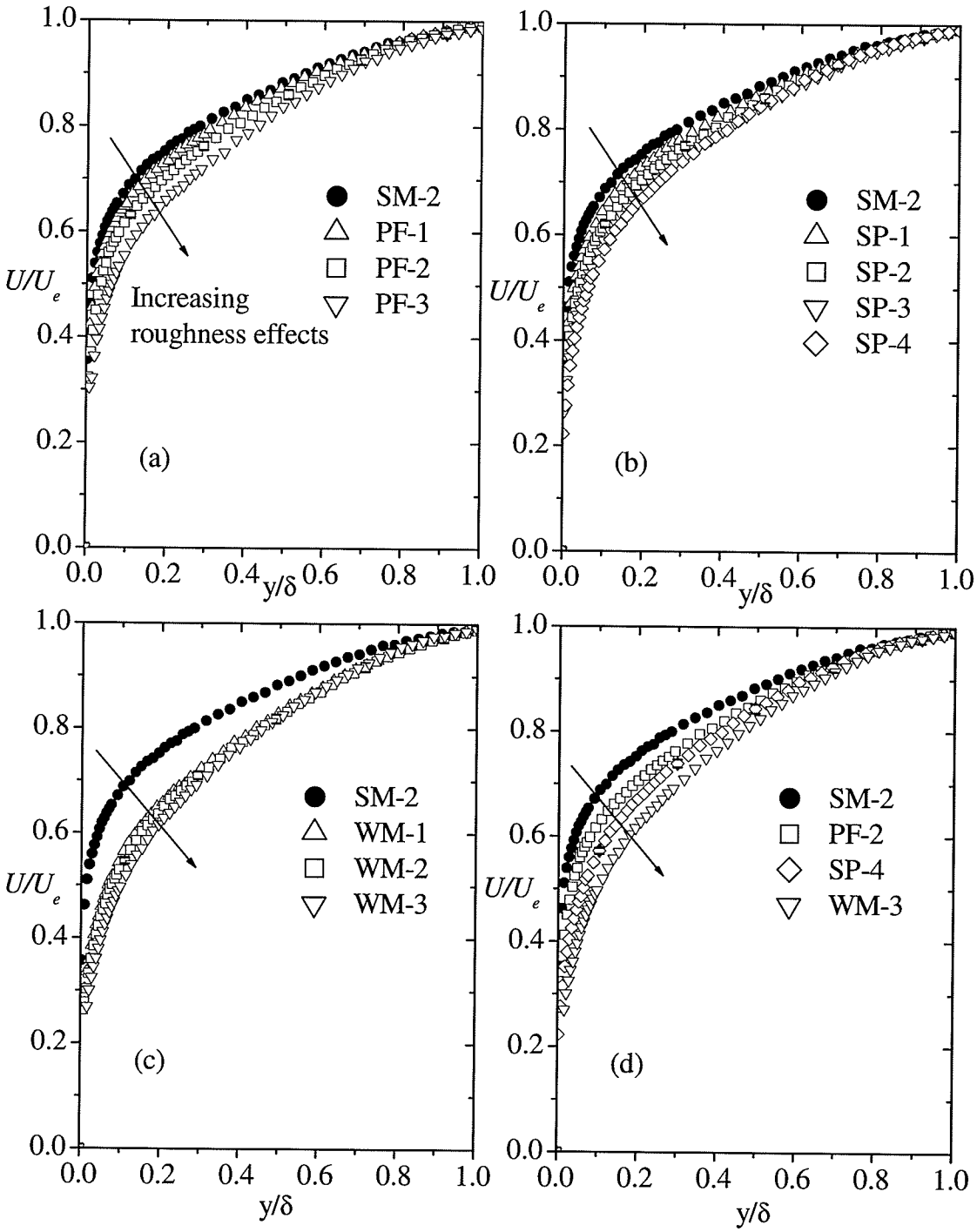

Figure 4-2: Mean velocity profiles over different rough surfaces using outer coordinates.

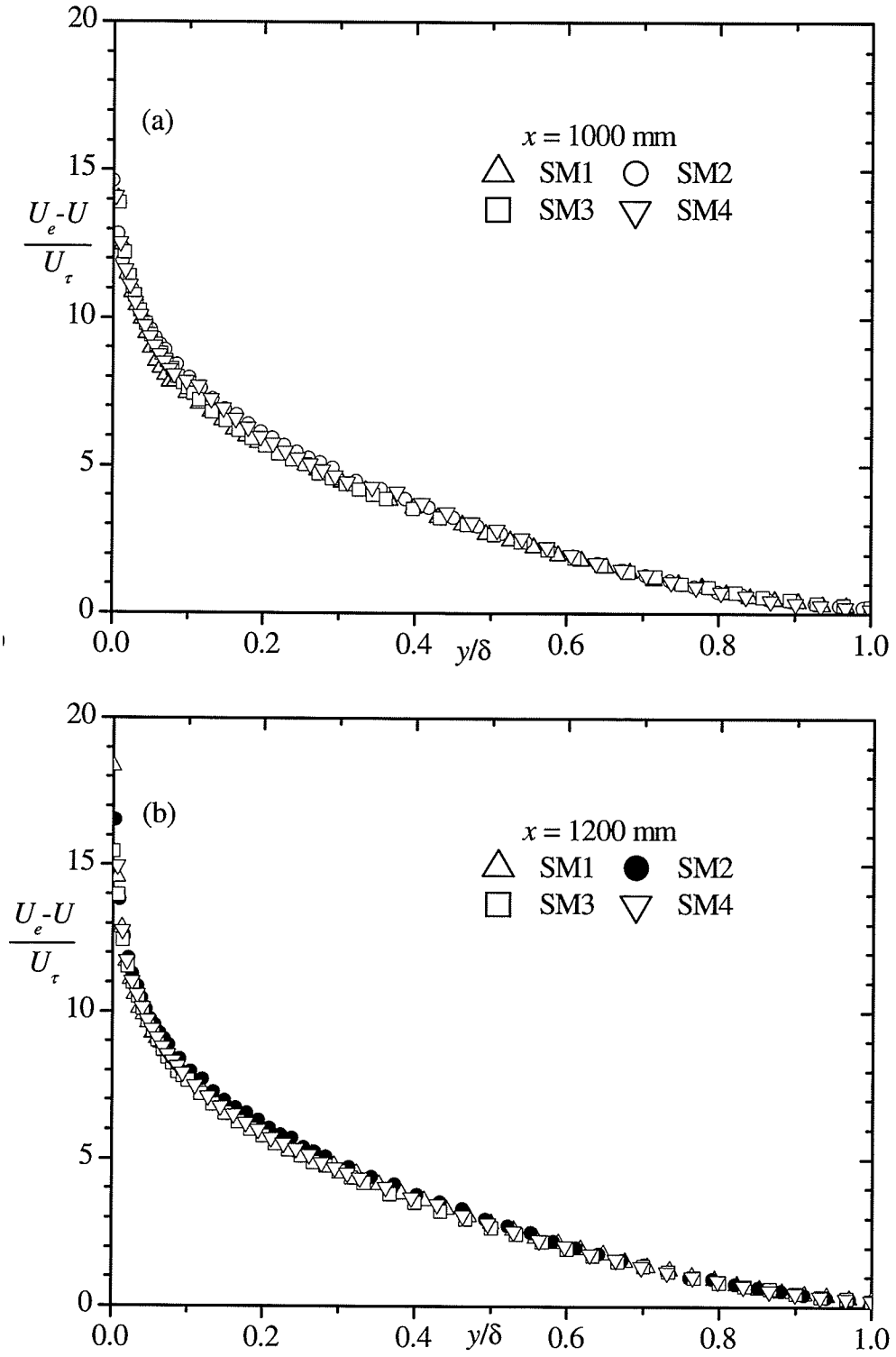

Figure 4-3: Mean velocity defect profiles at various Reynolds numbers using U_τ as the velocity scale.

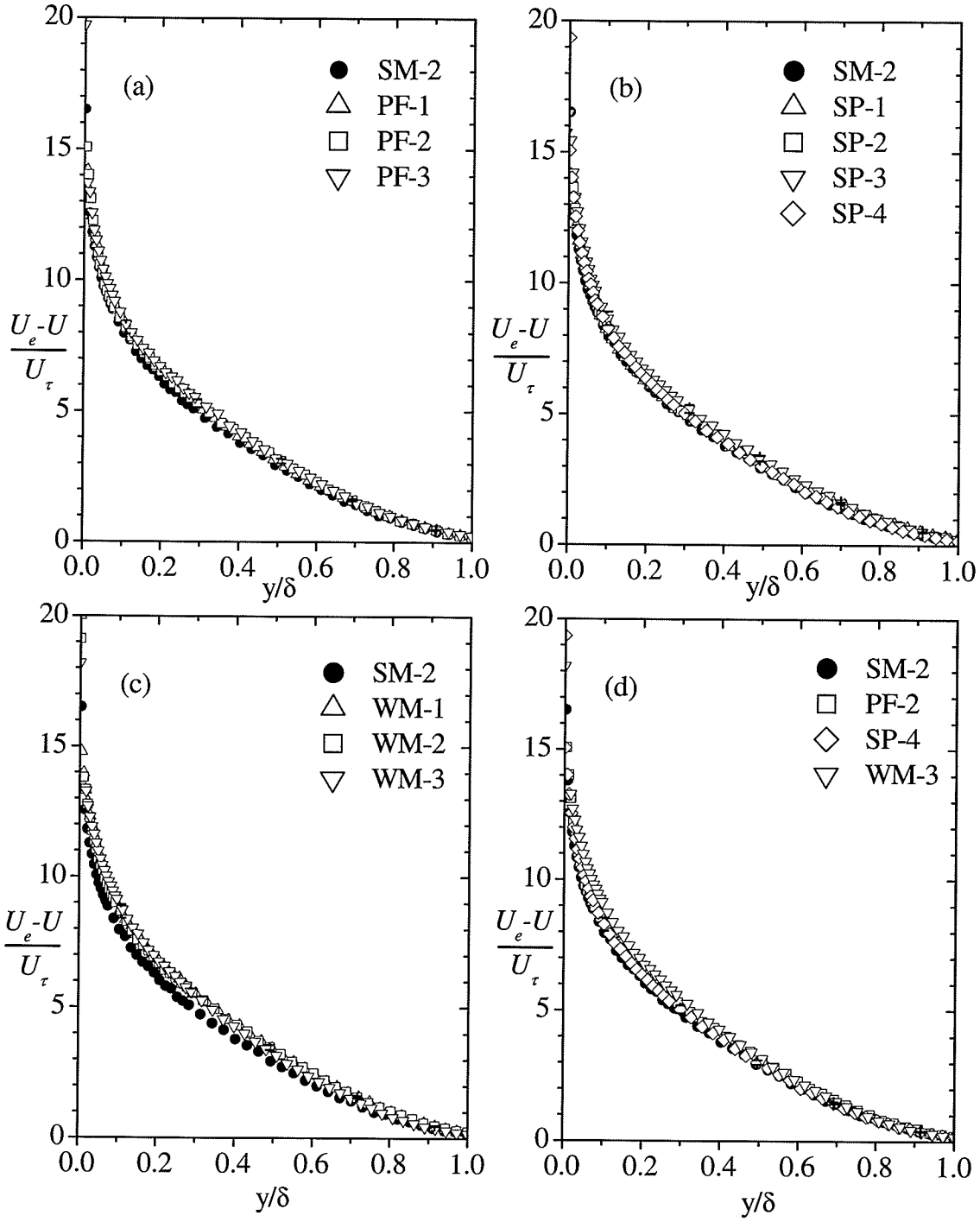

Figure 4-4: Mean velocity defect profiles over different rough surfaces using U_τ as the velocity scale.

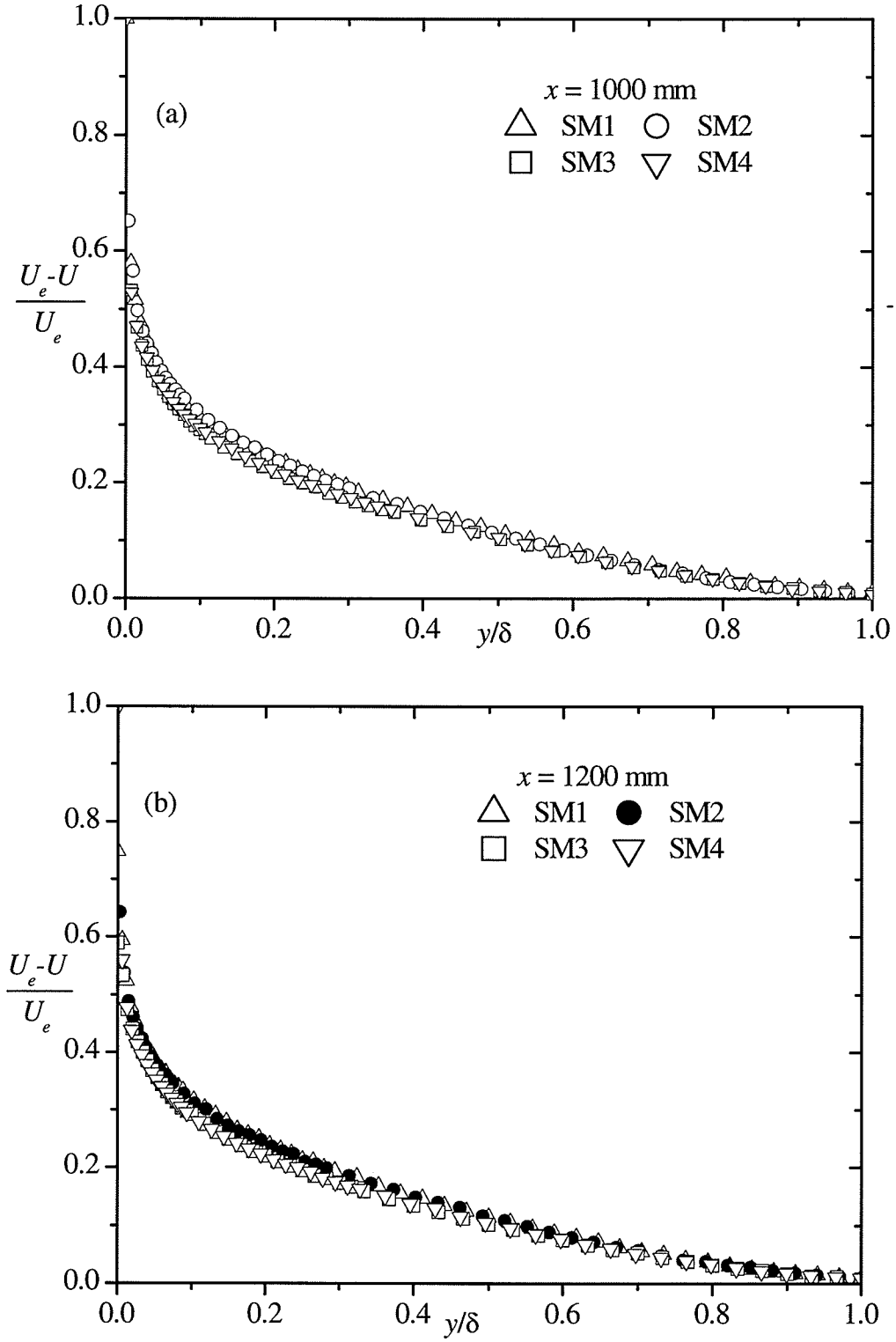

Figure 4-5: Mean velocity defect profiles at various Reynolds numbers using U_e as the velocity scale.

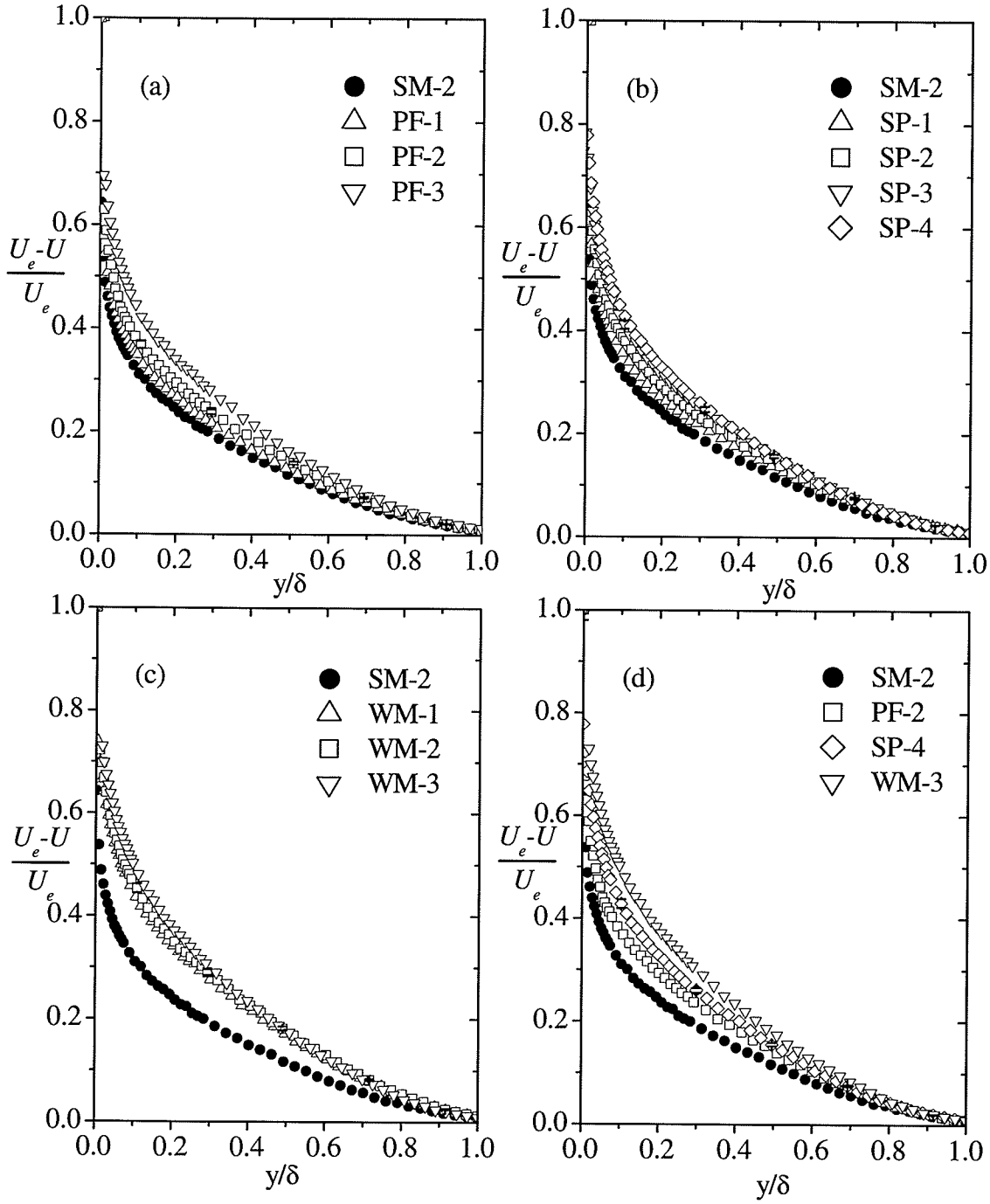

Figure 4-6: Mean velocity defect profiles over different rough surfaces using U_e as the velocity scale.

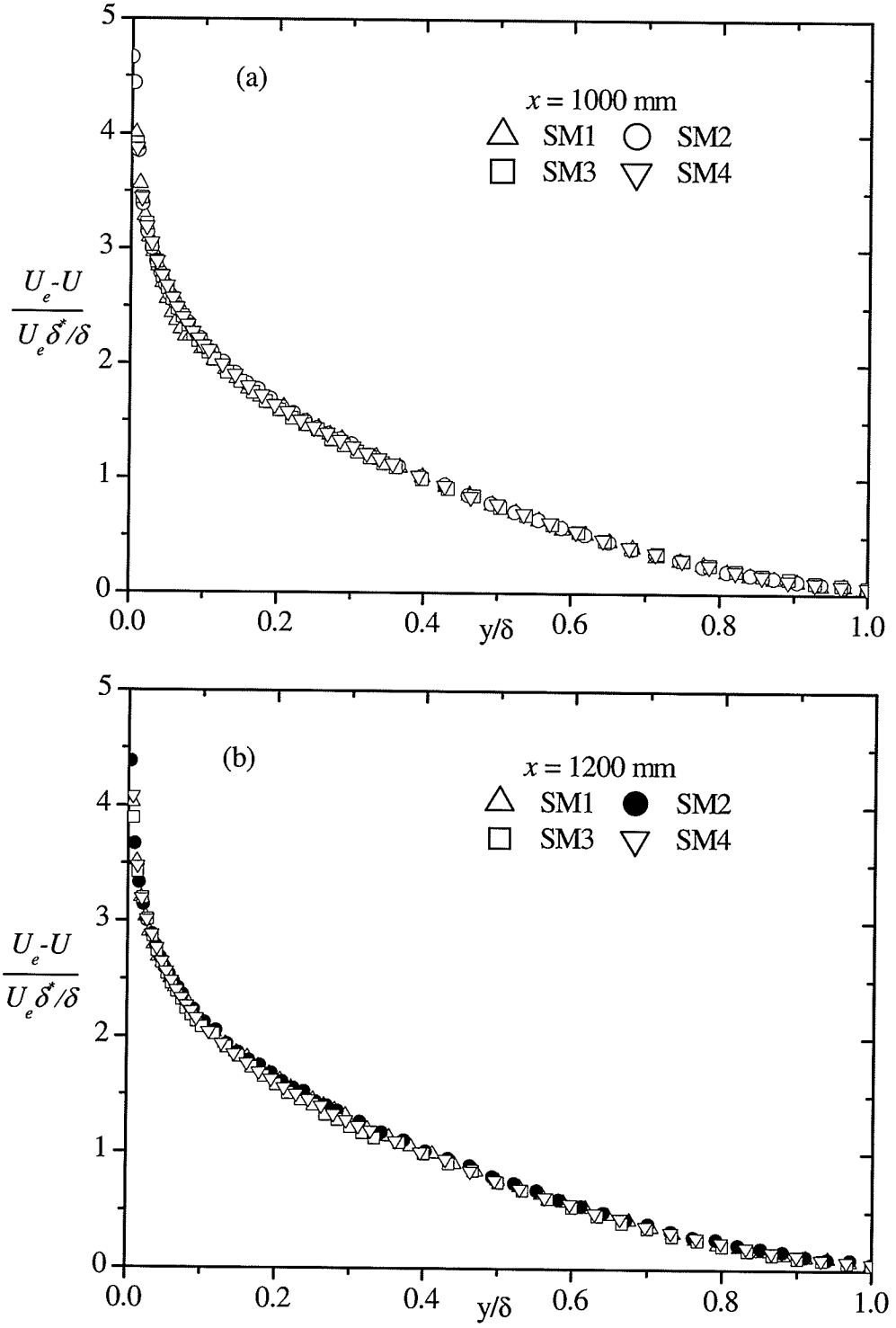

Figure 4-7: Mean velocity defect profiles at various Reynolds numbers using the scaling $U_e\delta^*/\delta$ proposed by Zagarola and Smits (1998).

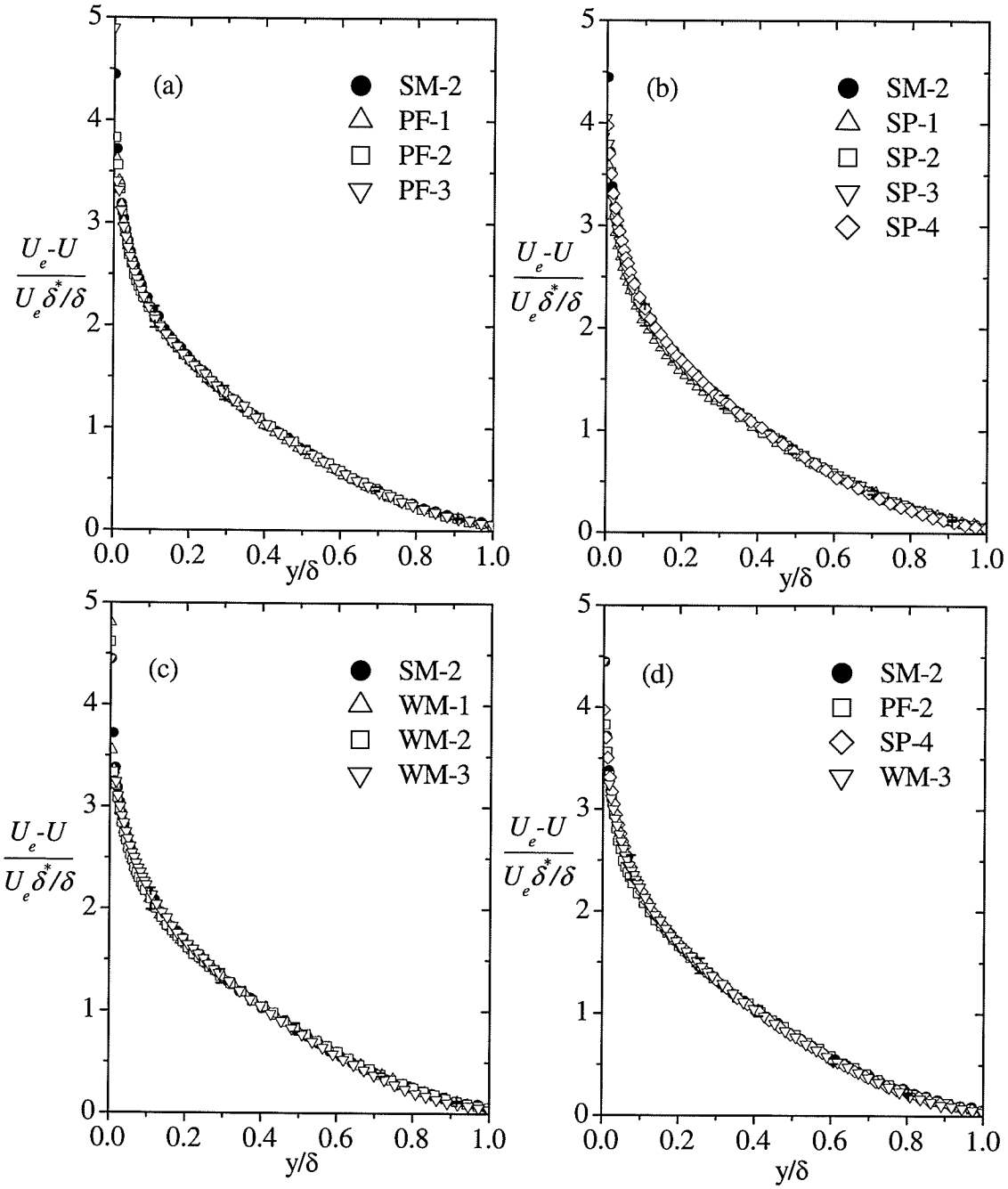

Figure 4-8: Mean velocity defect profiles over different rough surfaces using the scaling $U_e\delta^*/\delta$ proposed by Zagarola and Smits (1998).

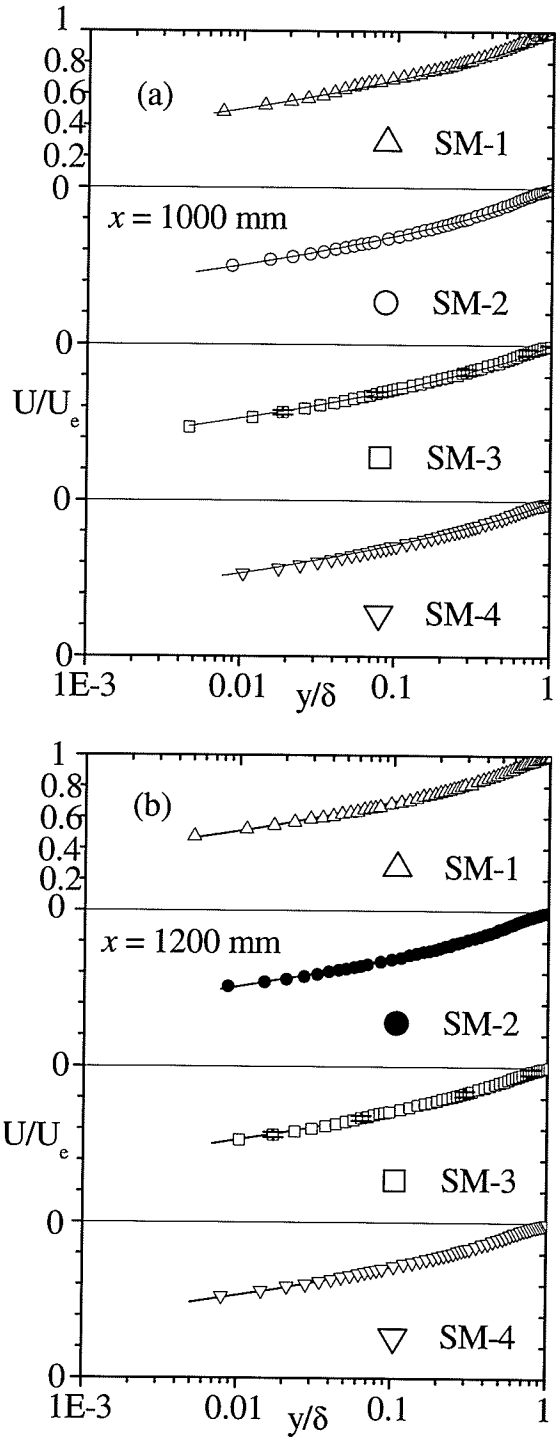

Figure 4-9: Mean velocity profiles at various Reynolds numbers in outer coordinates. Solid line is the power law fit (Eqn. 2.19 with B = 2.03).

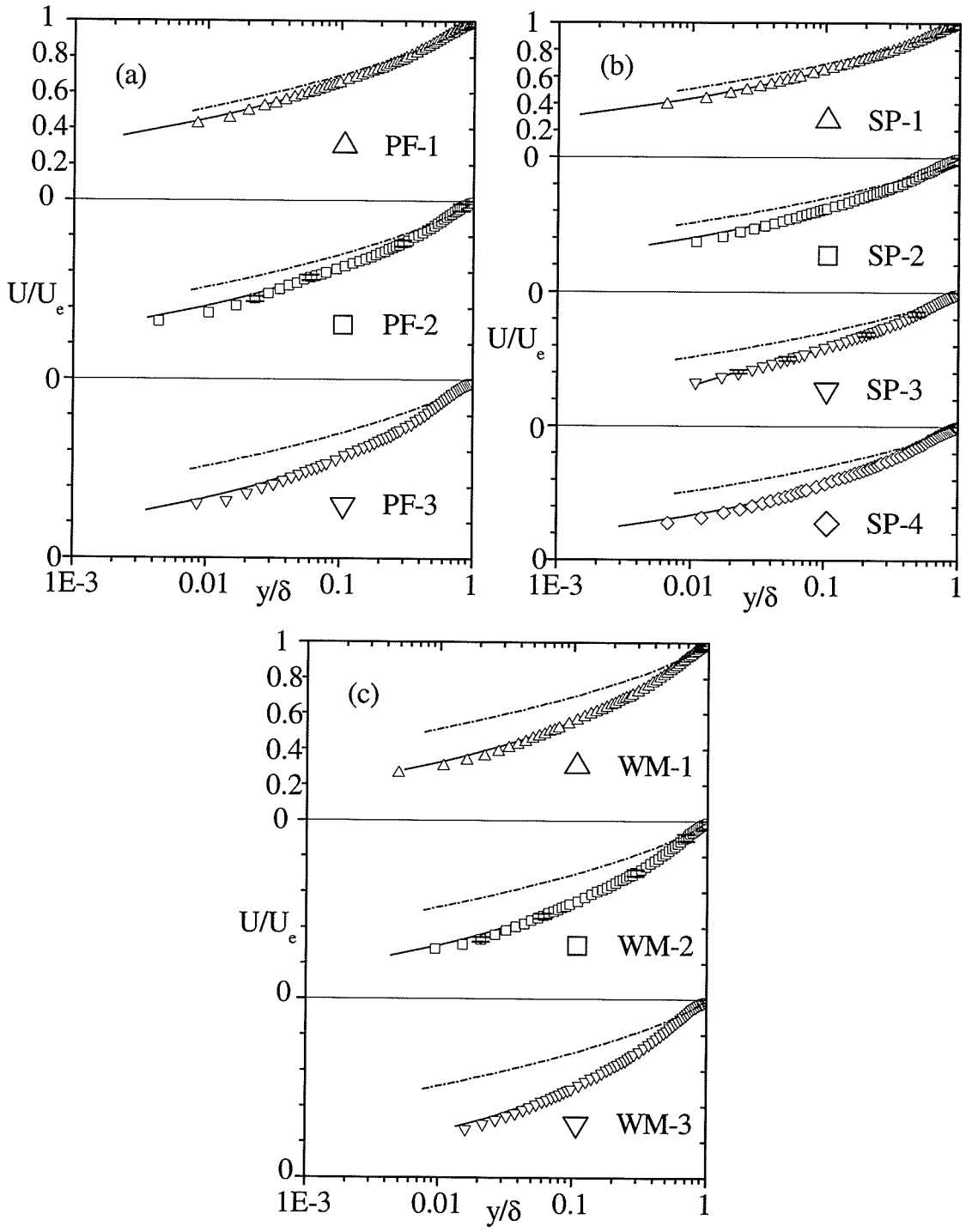

Figure 4-10: Mean velocity profiles over different rough surfaces in outer coordinates. Solid line is the power law fit (Eqn. 2.19 with B = 2.03), dash-dotted lines represent a reference smooth-wall power-law profile (SM-2).

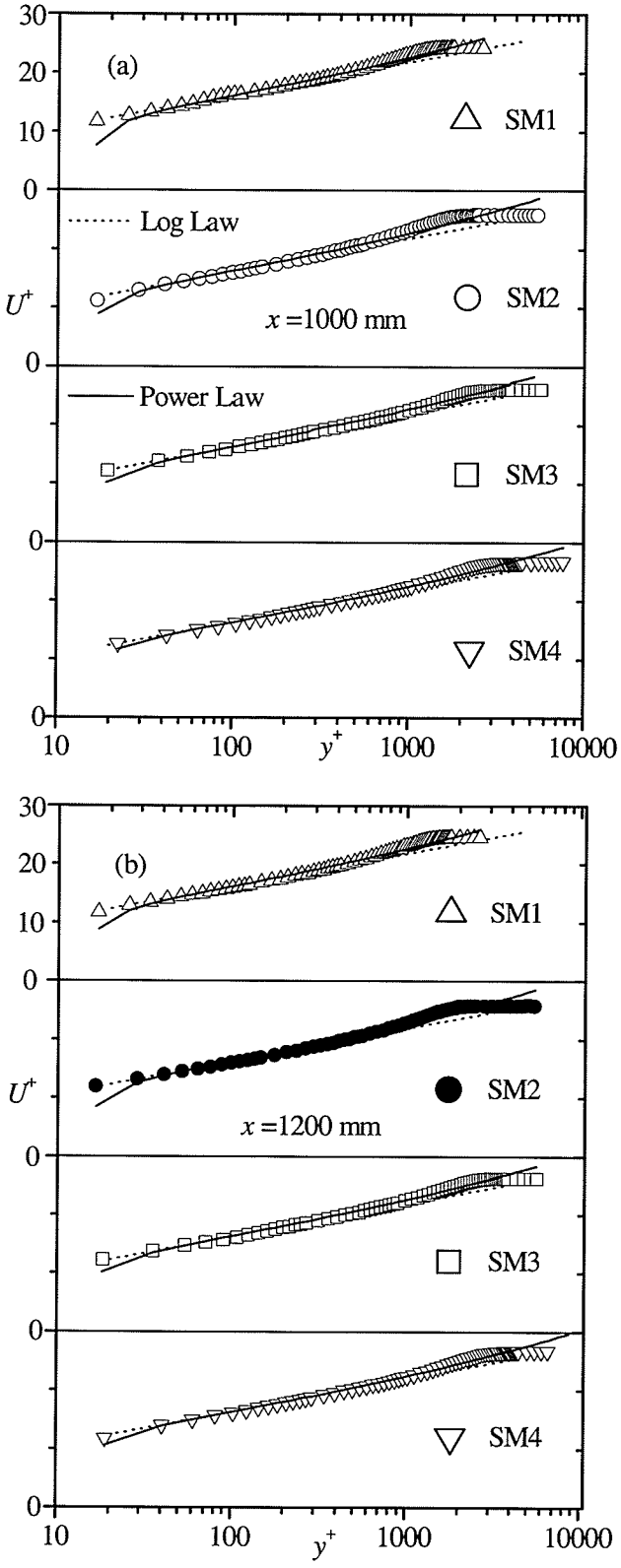

Figure 4-11: Mean velocity profiles at various Reynolds numbers in inner coordinates. Dotted lines correspond to log law (Eqn. 2.15), solid lines correspond to power law (Eqn. 2.17).

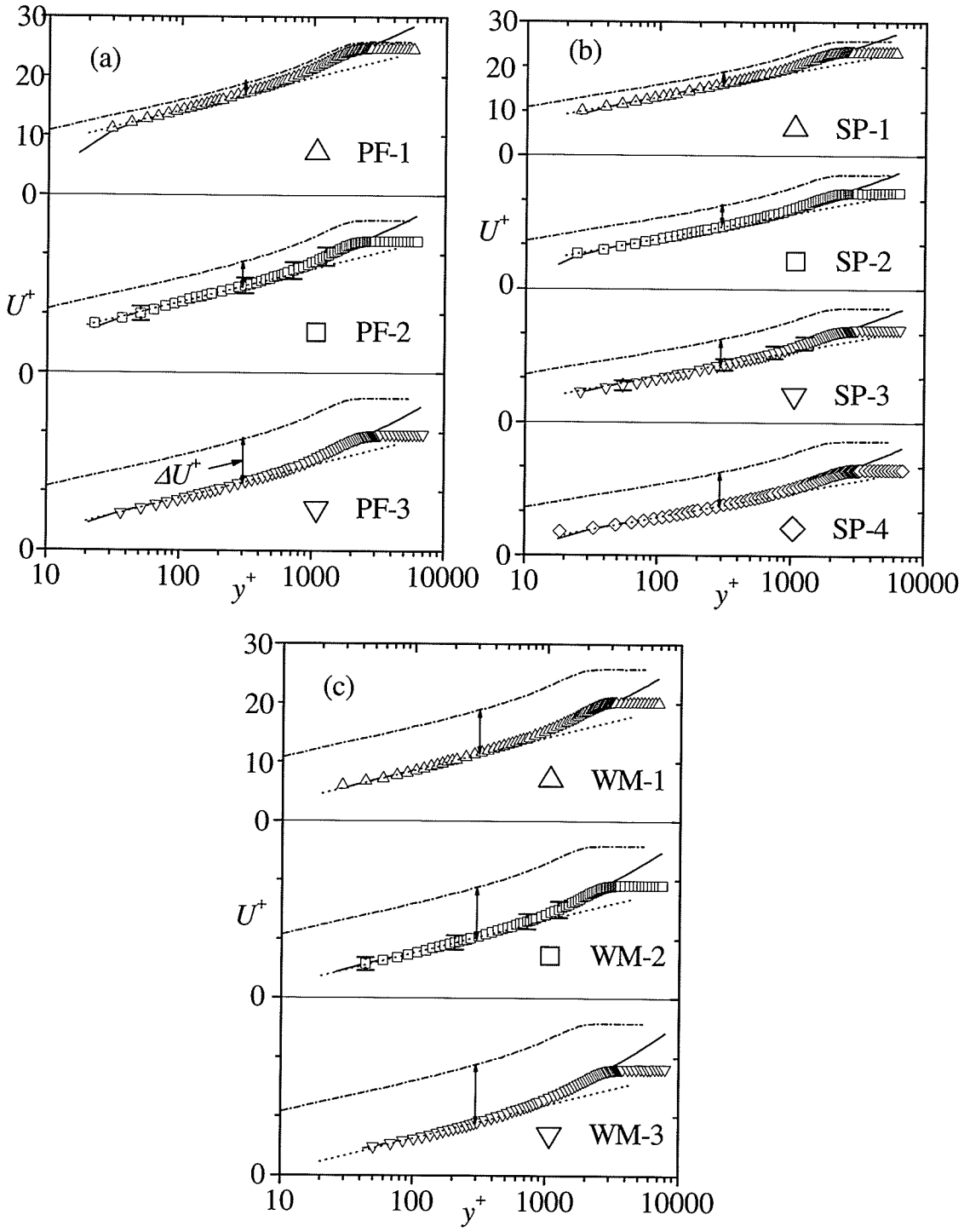

Figure 4-12: Mean velocity profiles over different rough surfaces in inner coordinates. Dotted lines correspond to log law (Eqn. 2.15), solid lines correspond to power law (Eqn. 2.17) and dash-dotted lines correspond to a reference smooth-wall log profile (SM-2).

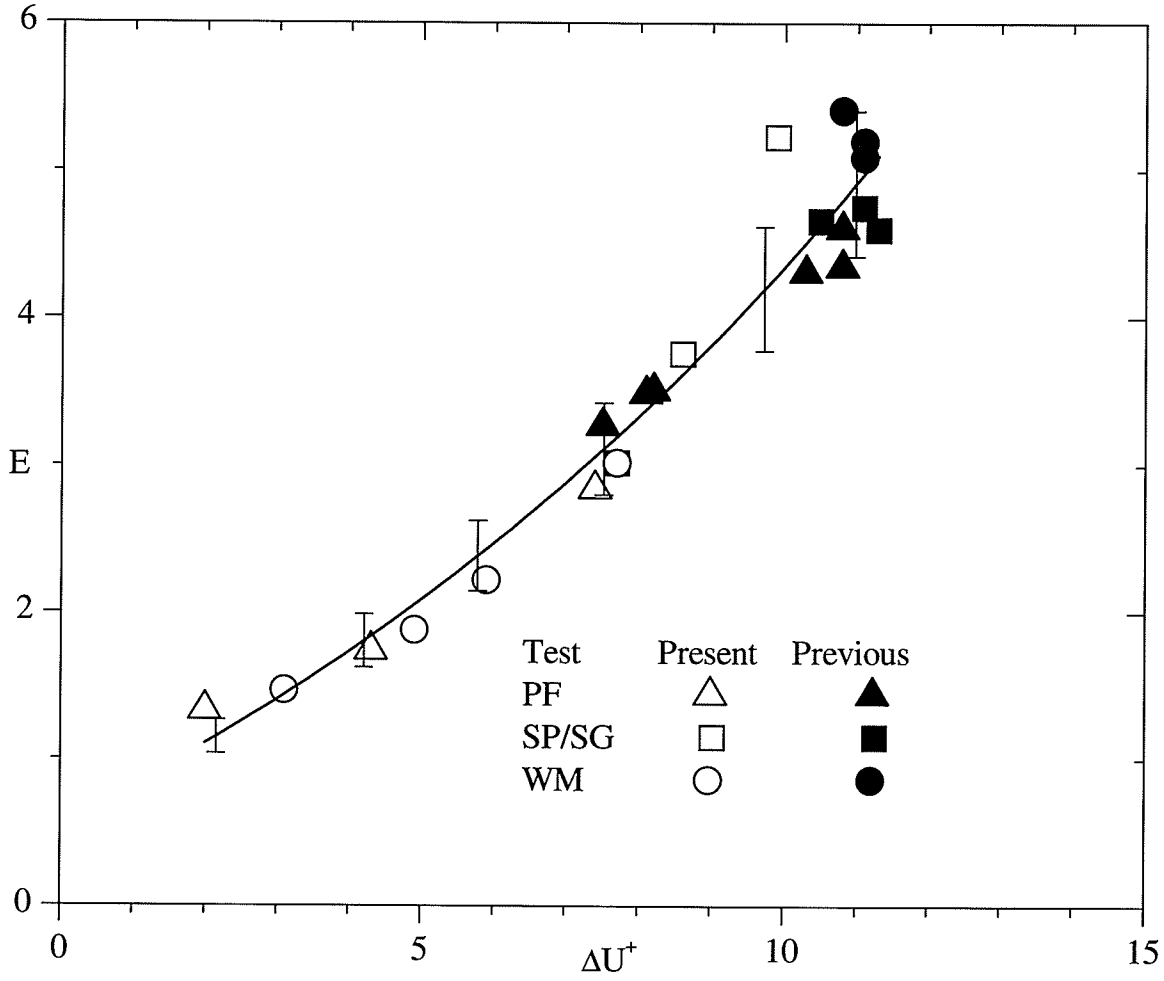

Figure 4-13: Variation of the power law parameter E proposed by Kotey *et al.* (2003) with roughness shift ΔU^+ for both transitionally rough and fully rough surfaces. Solid line is the best fit (Eqn. 4.1) to the data, and error bars denote a ± 10% deviation.

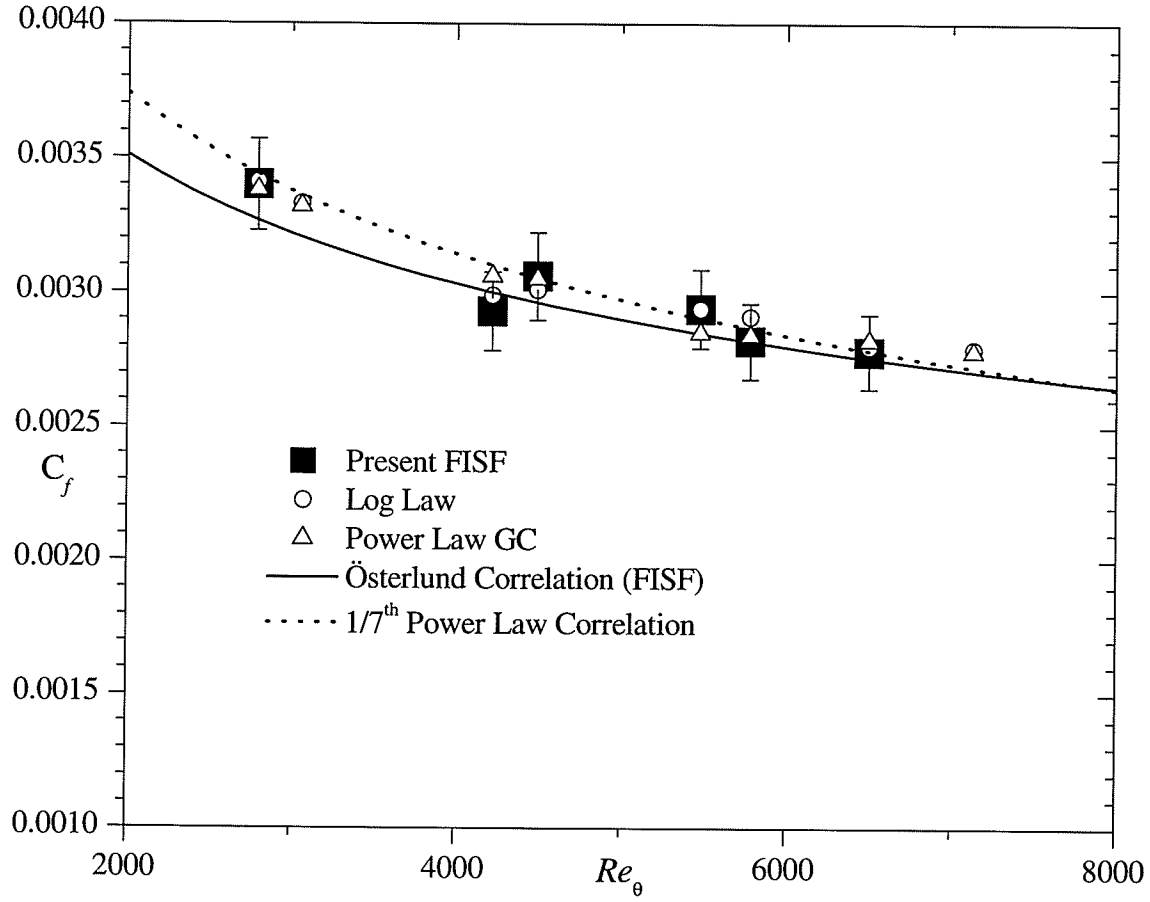

Figure 4-14: Comparison among smooth-wall skin friction values obtained using various techniques and correlations.

CHAPTER 5.0: SUMMARY, CONCLUSION AND RECOMMENDATIONS

5.1 Summary

This thesis reports measurements of the mean velocity profile in a canonical zero-pressure gradient turbulent boundary layer at moderate Reynolds numbers. The velocity measurements were obtained in a wind tunnel using a Pitot-probe in the range of $2700 < Re_\theta < 7900$. Skin friction characteristics in zero-pressure gradient turbulent boundary layers over a smooth surface, and transitionally rough and fully rough surfaces created from three geometrically different roughness elements were investigated.

Three different types of scaling were used to plot velocity defect profiles. The classical log law and power law proposed by George and Castillo (1997) was used to describe the mean velocity profile. The two techniques were used to obtain the corresponding skin friction values over smooth and rough surfaces. Secondly, an independent skin friction measuring technique, FISF, was applied to obtain skin friction on smooth surfaces, and the results are compared with values determined from the log law and power law.

5.2 Conclusion

The results presented in this thesis demonstrate that the mean velocity defect profiles show distinct Reynolds number and roughness effects when scaled with the freestream velocity U_e. Although the friction velocity U_τ was able to collapse mean velocity defect profiles obtained on a geometrically similar surface, it failed to collapse profiles over different surfaces. On the other hand, the defect profiles obtained at various Reynolds

number and geometrically different surfaces collapse reasonably well when scaled with $U_e\delta^*/\delta$.

The classical log law and power law formulation were shown to describe the overlap region of the mean velocity profile in a turbulent boundary layer quite well. For the smooth surface, the skin-friction values determined using the log law and power law are consistent with corresponding values determined from the fringe imaging skin friction technique. The log law and power law also predict similar skin friction values for the various rough surfaces studied in this work, and the main advantage of the power law over the log law is the ability of the power law to model a wider extent of the overlap region compared to the log law. It was also observed that the strength of wake (Π) were higher for rough surfaces when compared to values obtained for smooth surfaces.

5.3 Recommendations for Future Studies

Measurements of the fluctuating velocity field are required on the surfaces considered to further investigate the effects of smooth, transitionally rough and fully rough regimes on turbulent statistics.

REFERENCES

Andreopoulos J, Durst F, Zaric Z and Jovanovic J (1984) Influence of Reynolds number on characteristics of turbulent wall boundary layers. *Exp. Fluids.* **2**:7-16.

Akinlande OG, Bergstrom DJ, Tachie MF and Castillo L (2004) Outer flow scaling of smooth and rough wall turbulent boundary layers. *Expt. In Fluids* (Accepted for publication).

Barenblatt GI (1993) Scaling laws fro fully developed turbulent shear flows. Part1. Basic Hypothesis and Analysis. *JFM.* **248**:513-520

Bergstrom DJ, Tachie MF and Balachandar R (2001) Application of power laws to low Reynolds number boundary layers on smooth and rough surfaces. *Phy. of Fluids.* **13**(11): 3277-3284.

Bergstrom DJ, Kotey NA and Tachie MF (2002) The effects of surface roughness on the mean velocity profile in a turbulent boundary layer. *J. Fluids Eng* **124**:664-670.

Bourassa C, Thomas FO and Nelson RC (2000) Oil film interferometry in a turbulent boundary layer undergoing relaminarization. *9th Int'l Symp. On Flow Visualization.*

Castillo L and Walker DJ (2002) Effect of upstream conditions on the outer flow of turbulent boundary layers. *AIAA* **40**:1292-1299.

Coles DE (1956) The law of the wake in the turbulent boundary layer. *J. Fluid Mech.* **1**:191-226.

Coles DE (1962) The turbulent boundary layer in a compressible fluid," *Rand Corp Report* no. R-403-PR, Santa Monica, CA.

Degraaff BD (1999) Reynolds number scaling of the turbulent boundary layer on a flat plate and on swept and unswept bumps. *PhD. Thesis*, Stanford.

Fernholz HH and Finley PJ (1996) The incompressible zero pressure gradient turbulent boundary layer: an assessment of the data. *Prog. Aerospace Sci.* **32**:245-311.

Finley PJ, Khoo Chong Phoe and Chin Jeck Poh (1966) Velocity measurements in a thin turbulent wake layer. *La Houille.* **21**:713-721.

Furuya Y and Fujita H (1967) Turbulent boundary layers on a wire-screen roughness. *JSME.* **10**:77-86.

Gad-el-Hak M and Bandyopadhyay PR (1994) Reynolds number effects in wall-bounded flows. *Applied Mech. Rev.* **47**(8): 307-364.

George WK and Castillo L (1997) Zero-pressure gradient turbulent boundary layer. *Appl. Mech. Rev.* **50**(11):689-729.

Granville PS (1977) Drag and turbulent boundary layer of flat plates at low Reynolds numbers. *J. Ship. Res.* **21**:30-39.

Haritonidis JH (1989) The measurement of wall shear stress. *Adv. Fluid Mech.* 229-261.

Jiménez J (2004) Turbulent flows over rough walls. *Annu. Rev. Fluid Mech.* **36**:173-196.

Knight D and Degrez G (1998) Shock wave boundary layer interactions in high Mach number flows – a critical survey of current CFD prediction capabilities. *AGARD Advisory Report* AP-319 **11**.

Kotey NA, Bergstrom DJ and Tachie MF (2003) Power laws for rough wall turbulent boundary layers. *Phys of Fluids* 15(6):1396-1404.

Krogstad PA, Antonia RA and Browne LWB (1992) Comparison between rough and smooth wall turbulent boundary layers. *J. Fluid Mech.* **245**:599-617.

Krogstad PA and Antonia RA (1999) Surface roughness effects in turbulent boundary layers. *Expt. Fluids* **27**:450-460.

Krogstad PA and Antonia RA (2001) Turbulence structure in boundary layers over different types of surface roughness. *Fluid Dynamics Research.* **28:**139-157.

Landweber L (1953) The frictional resistance of flat plates at zero pressure gradient. *Trans. Soc. Nav. Arch. Mar. Eng.* **61**:5-32.

Mabey DG (1979) Influence of the wake component on turbulent skin friction at subsonic and supersonic speeds. *Aeronaut Quart.* **30:**590-606.

MacMillan FA (1956) Experiments on Pitot-tubes in shear flow. *Aero. Res. Counc.* R & M. 3028.

Milikan CB (1938) A critical discussion of turbulent flows in channels and circular tubes. *Proceedings of the 5th Int'l Congress of App. Mech.*

Moffat R (1988) Describing the uncertainties in experimental results. *Experimental Thermal and Fluid Science.* **1**:3-17.

Naughton JW and Sheplak M (2002) Modern developments in shear-stress measurement. *Prog Aero Sci.* **38**:515-570.

Österlund JM, Johansson AV, Nagib HM, Hites, MH (1999) Wall shear stress measurements in high Reynolds number boundary layers from two facilities. *30th AIAA* Fluid Dynamics Conference, 28 June - 1 July, Norfolk, Virginia.

Perry AE, Schofield WH and Joubert PN (1969) Rough wall turbulent boundary layers. *J. Fluid Mech.* **37:**383-413.

Prandtl L (1932) Zur Turbulenten Strömung in Roren und längs Platten. *Ergeb Aerod Versuch Göttingen,* IV Lieferung, 18.

Preston JH (1958) The minimum Reynolds number for a turbulent boundary layer and the selection of a transition device. *J. Fluid Mech.* **3**:373-384.

Preston JH and Sweeting NE (1944) The velocity distribution in the boundary layer of a plane wall at high Reynolds numbers with suggestions for further experiments. *Aeronaut Res. Council Report* no. ARC-FM-671, London.

Purtell LP, Klebanoff PS and Buckley FT (1981) Turbulent boundary layer at low Reynolds number. *Phys. Fluids.* **24**(5):802-811.

Raupauch MR, Antonia RA and Rajagopalan S (1991) Rough-wall turbulent boundary layers. *Appl. Mech. Rev.* **44**:1-25.

Reynolds O (1883) An experimental investigation of the circumstances which determine whether the motion of water shall be direct or sinuous and of the law of resistance in parallel channels. *Phil. Trans. Roy. Soc. Lond.* ser A **174**:935-982.

Saddoughi SG and Veeravalli SV (1994) Local isotropy in turbulent boundary layers at high Reynolds number. *J. Fluid Mech.*

Schlichting H (1968) Boundary layer theory. *New York: McGraw-Hill.* 6th Edition.

Seo J (2003) Investigation of the upstream conditions and surface roughness in turbulent boundary layer. Ph.D. thesis, Rensselaer Polytechnic Institute, NY.

Simpson RL (1970) Characteristics of turbulent boundary layers at low Reynolds numbers with and without transpiration. *J. Fluid Mech.* **42**:769-802.

Simpson RL (1976) Comment on 'Perdition of Turbulent boundary layers at low Reynolds numbers.' *AIAA.* **14**:1662-1663.

Smith DW and Walker JH (1959) Skin-friction measurements in incompressible flow. *NACA Report* No R-26, Washington DC.

Tachie MF, Bergstrom DJ, Balachandar R (2000) Rough wall turbulent boundary layers in shallow open channel flow. *J. Fluids Eng.* **122**:533-541.

Tennekes H and Lumley JL (1972) A first course in turbulence. *MIT Press*, Cambridge MA.

Todd FH (1951) Skin friction resistance and the effect of the surface roughness. *Trans. SNAME.* **59**:315.

White FM (1991) Viscous fluid flow. *Boston, Mass., McGraw Hill*, 2nd Edition.

White FM (1986) Fluid Mechanics. *New York, McGraw-Hill*, 2nd Edition.

Winter KG (1997) An outline of the techniques available for the measurement of skin friction in turbulent boundary layers. *Prog. Aero Sci* 18:1-57.

Zagarola MV Perry AE and Smits AJ (1997) Log laws or power laws: The scaling in the oerlap region. *Phys. Fluids.* **9**(7):2094-2100.

Zagarola MV and Smits AJ (1998) Mean-flow scaling of turbulent pipe low. *J. Fluid Mech.* **373**:33-79.

Zilliac GG (1996) Further developments of the fringe-imaging skin friction technique. *NASA TM 110425*.

Zilliac GG (1999) The fringe-imaging skin friction technique PC application user's manual. *NASA TM 208794*.

APPENDIX A

A personal computer application, CXWIN4G, is designed to extract skin friction measurements from fringes formed on the model surface of a wind tunnel following the procedure given below.

Reading an image: To acquire an image into the software for processing,

1. Left-double click on the CXWIN4G icon.
2. Left-click on the "Read File" button in the main CXWIN4G window.
3. In the "Data" popup, enter the oil kinematic viscosity and refractive index, wavelength of light source data, and total run time. For the dynamic freestream properties, select "*q,t*" (dynamic pressure and temperature) and enter the values.
4. Pixel line width of 10 was selected to increase the accuracy of the analysis.
5. In "Appended char." field, enter the reference name for this analysis.
6. Click OK.
7. In the "Read an Image From a File" popup dialog box, select the appropriate TIF image and click "Open."

Image Spatial Calibration: Image calibration (or camera calibration) is necessary to map pixels in the image to physical coordinates on a surface.

1. Switch the image to high resolution mode by pressing Esc button.

2. Click on the "Calibrate" button at the top of the main window. In the popup dialog box, select the coordinate plane, which most closely parallels that of the image, (i.e., *XY*, *XZ* or *YZ*) should be selected. Also, in this dialog box, enter the distance of camera (in inches) from the model plane.
3. Position the cross cursor over the first calibration point (a point in the image where *X*, *Y*, *Z* location is known) and left-click. A popup dialog box will appear and *X*, *Y*, and *Z* coordinates (in inches) of the calibration point should be entered. Repeat step 3 and to enter more calibration points (minimum of 6 points desired).
4. Right-click on the image when all of the calibration points have been entered. A "Calibration Complete" message should appear. The calibration data will then be automatically stored in default.bas (the CXWIN4G data base file).

Find the Fringe Intensity Distribution: The fringe intensity distribution is found by drawing a line normal to the fringe fronts starting upstream of the oil flow and extending downstream of the second fringe.

1. While the image is in the high resolution mode, place the cursor upstream of the first fringe and left-click.
2. Move the cursor to a point downstream of the second fringe and left-click.
3. Right-click and the intensity distribution (along the line drawn on the fringe) should appear in the upper-right child window (see Figure A-1).

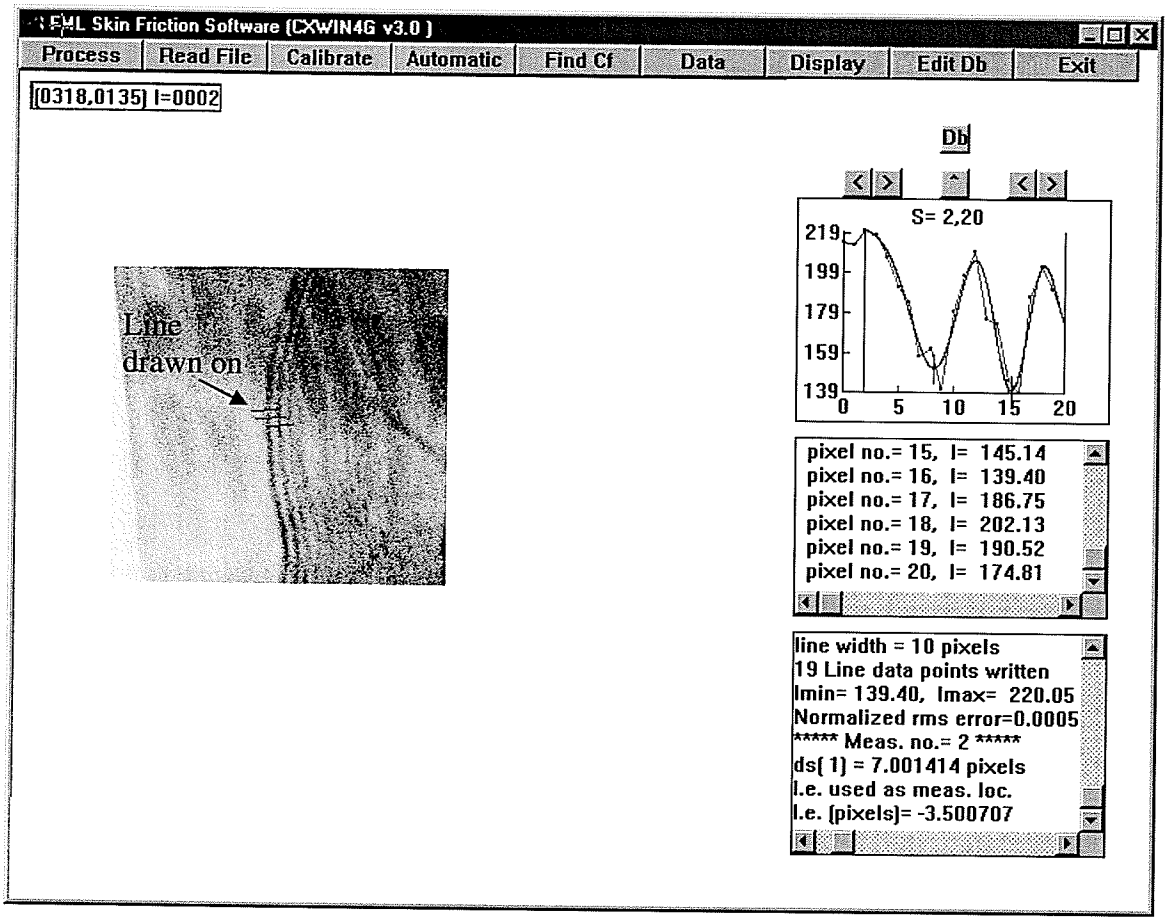

Figure A-1: Main window of FISF software showing a sample semi-processed image.

Measure the Fringe Spacing: A nonlinear regression algorithm developed specifically for interferometry is applied in this step to determine the fringe spacing.

1. Click on the "Find C_f" button at the top of the main window and the fringe spacing (in pixels) will appear in the lower-right child window.
2. If the regression results (shown in the upper-right window; (see Figure A-1) are acceptable, click on the "Db" button to store this particular measurement in the database.

Figure A-1 also shows the fringe pattern intensity distribution (the upper-right child window), intensity peak-to-peak, $I_{p\text{-}p}$, and normalized rms error of the processed image (bottom-right child window). For the image shown, $I_{p\text{-}p} \approx 80$. A high $I_{p\text{-}p}$ indicates the suitability of the candidate surface and also, overall accuracy of an FISF measurement is directly related to this quantity (Zilliac, 1999).

Process the Data: In this step the data stored in the default.bas file is analyzed.

1. Click on the Process button at the top of the main window.

Skin Friction Magnitude: Skin friction value obtained from the software analysis is stored in file named "photo.out" and can be opened using any text editor.

APPENDIX B

Sample Calculations for the Error Analysis

A sample calculation for the error analysis, describing the method of estimating uncertainty in the experimental data, is presented in this Appendix. The procedure is outlined by (Moffat, 1988) was used in estimating these uncertainty bounds.

n_o	= 1.40300	$\pm$ 2.1000 x 10^{-4}	
μ_o	= 0.10184	$\pm$ 1.5280 x 10^{-3}	[Pa.s]
q_∞	= 650.120	$\pm$ 6.5012	[Pa]
t	= 308.000	$\pm$ 6.1600	[sec]
λ	= 542 x 10^{-9}	Negligible	[m]
Δs	= 0.00112	$\pm$ 3.9158 x 10^{-5}	[m]

The above data is for the experimental run at U_e = 34 m/s at x = 1000 mm. We wish to estimate the uncertainty in the skin friction values obtained by FISF technique.

The governing equation for skin friction based on FISF technique (Eqn. 2.23) is given by

$$Cf = \frac{2n_o\mu_o}{q_\infty t\lambda}\Delta s \cdot \qquad (2.23)$$

Following the procedure in Moffat (1988), C_f is a given function of n_o, μ_o, q_∞, t, λ and Δs. Thus,

$$C_f = C_f(n_o, \mu_o, q_\infty, t, \lambda, \Delta s) \tag{A.1}$$

and the uncertainty in C_f is defined as

$$\omega_{Cf} = \left[\left(\frac{\partial C_f}{\partial n_o}\omega_{n_o}\right) + \left(\frac{\partial C_f}{\partial \mu_o}\omega_{\mu_o}\right) + \left(\frac{\partial C_f}{\partial q_\infty}\omega_{q_\infty}\right) + \left(\frac{\partial C_f}{\partial t}\omega_t\right) + \left(\frac{\partial C_f}{\partial \lambda}\omega_\lambda\right) + \left(\frac{\partial C_f}{\partial \Delta s}\omega_{\Delta s}\right)\right]. \tag{A.2}$$

Now evaluate the uncertainty in each term when the nominal value of C_f is 0.00294:

$$\frac{\partial C_f}{\partial n_o} = \frac{2\mu_o}{q_\infty t\lambda}\Delta s = \frac{2\times 0.101843}{650.12\times 308\times 542\times 10^{-9}}0.001118 = 2.0997628\times 10^{-3}$$

$$\frac{\partial C_f}{\partial \mu_o} = \frac{2n_o}{q_\infty t\lambda}\Delta s = \frac{2\times 1.403}{650.12\times 308\times 542\times 10^{-9}}0.001118 = 0.0289265$$

$$\frac{\partial C_f}{\partial q_\infty} = \frac{2n_o\mu_o}{q_\infty^2 t\lambda}\Delta s = \frac{2\times 1.403\times 0.101843}{650.12^2\times 308\times 542\times 10^{-9}}0.001118 = 4.5314197\times 10^{-6}$$

$$\frac{\partial C_f}{\partial t} = \frac{2n_o\mu_o}{q_\infty t^2\lambda}\Delta s = \frac{2\times 0.101843}{650.12\times 308^2\times 542\times 10^{-9}}0.001118 = 9.564826\times 10^{-6}$$

$$\frac{\partial C_f}{\partial \lambda} = \frac{2\mu_o}{q_\infty t\lambda^2}\Delta s = \frac{2\times 0.101843}{650.12\times 308\times (542\times 10^{-9})^2}0.001118 = 5479.704797$$

$$\frac{\partial C_f}{\partial \Delta s} = \frac{2n_o\mu_o}{q_\infty t\lambda} = \frac{2\times 1.403\times 0.101843}{650.12\times 308\times 542\times 10^{-9}} = 2.633104$$

Using Eqn. B.2, thus the uncertainty interval in C_f is

$$\omega_{Cf} = 1.30\times 10^{-4}$$

and the fractional uncertainty interval in C_f is

$$\frac{\omega_{Cf}}{C_f} = \frac{1.30\times 10^{-4}}{0.00294}\times 100 = 4.42\%\cdot$$